2017년 2월

석사학위 논문

# Modulation of Organic-Inorganic Hybrid Ternary Heterojunction for Improved Efficiency of Organic Solar Cells

조 선 대 학 교 대 학 원

탄 소 소 재 학 과

정 한 빈

# Modulation of Organic-Inorganic Hybrid Ternary Heterojunction for Improved Efficiency of Organic Solar Cells

유기-무기 하이브리드 삼중접합 나노구조를 통한
유기태양전지 효율향상에 관한 연구

2017년 2월 24일

조 선 대 학 교 대 학 원

탄 소 소 재 학 과

정 한 빈

# Modulation of Organic-Inorganic Hybrid Ternary Heterojunction for Improved Efficiency of Organic Solar Cells

지도교수 이 재 관

이 논문을 이학석사학위신청 논문으로 제출함.

2016년 10월

조 선 대 학 교 대 학 원

탄 소 소 재 학 과

정 한 빈

# 정한빈의 석사학위논문을 인준함

위원장 조선대학교 교수 김 호 중 (인)

위 원 조선대학교 교수 손 홍 래 (인)

위 원 조선대학교 교수 이 재 관 (인)

2016년 11월

## 조 선 대 학 교 대 학 원

# TABLE OF CONTENTS

**List of tables** ····· III

**List of figures** ····· IV

**Abstract** ····· VIII

**Chapter 1.** ····· 1

**Organic-Inorganic Hybrid Ternary Bulk Heterojunction of Nanostructured Perovskite-Low Bandgap Polymer-PCBM for Improved Efficiency of Organic Solar Cells**

**A. Introduction** ····· 2

**B. Experimental methods** ····· 6
1. Materials
2. Measurements and instruments.
3. Device fabrication.

**C. Result and discussion** ····· 8

**D. Conclusion** ····· 28

**E. Reference** ····· 29

**Chapter 2.** ····· 31

**Improved Efficiency of Solution-Processed Bulk-Heterojunction Organic Solar Cells and Planar-Heterojunction Perovskite Solar Cells with Efficient Hole-Extracting Si Nanocrystals**

**A. Introduction** ····· 32

**B. Experimental methods** ····· 36
1. Materials
2. Preparation of Si NCs
3. Measurements and instruments

4. Device fabrication

**C. Result and discussion** ····· **39**

**D. Conclusion** ····· **56**

**E. Reference** ····· **57**

**List of publications** ····· **60**

**List of poster** ····· **61**

# LIST OF TABLES

**Table 1.1** Photovoltaic performances of solar cell devices fabricated with $MAPbI_3$ perovskite, PCPDTBT, and PCBM.

**Table 2.1** Photovoltaic performances of these BHJ OSC (black) and PHJ PrSC (red) devices with PEDOT:PSS/p-Si NC HEM layers fabricated at various concentrations (0, 0.024, 0.034, 0.057, 0.171, and 0.854 mg/ml) of Si NCs in CB solvent.

**Table 2.2** Photovoltaic performances of BHJ OSCs and PHJ PrSCs fabricated with/without Si NCs HEMs cast on ITO/PEDOT:PSS.

# LIST OF FIGURES

Figure 1.1 Schematic descriptions for (a) preparation of nanostructured $MAPbI_3$-PCPDTBT-PCBM TBHJ film on ITO/PEDOT:PSS substrate, (b) TBHJ hybrid solar cell device structure, and (c) charge transfers in simplified TBHJ interfaces of (1) PCPDTBT-PCBM, (2) PCBM-$MAPbI_3$-PCPDTBT, and (3) $MAPbI_3$-PCBM.

Figure 1.2 FESEM surface images of $MAPbI_3$ materials, which were fabricated by caring the concentration (a) 0, (b) 1, (c) 3, (d) 5, (e) 7, and (f) 10 wt% of $MAPbI_3$ perovskite precursor in DMF solvent, spin-cast on the ITO/PEDOT:PSS substrate.

Figure 1.3 FESEM surface images and EDAX analysis of $MAPbI_3$ materials, which were fabricated by caring the concentration (3 wt%) of $MAPbI_3$ perovskite precursor in DMF solvent, spin-cast on the ITO/PEDOT:PSS substrate.

Figure 1.4 XRD patterns of $MAPbI_3$ materials, which were fabricated by caring the concentration (1, 3, 5, 7, and 10wt%) of $MAPbI_3$ perovskite precursor in DMF solvent, spin-cast on the ITO/PEDOT:PSS substrate.

Figure 1.5 (a) Photovoltaic performances of TBHJ hybrid solar cell devices fabricated from PCPDTBT-PCBM BHJ film with DIO additive using $MAPbI_3$ perovskite precursor of the various concentration (0, 1, 3, 5, 7, and 10 wt%) in DMF solvent and (b) XRD patterns of $MAPbI_3$ nano dots cast on ITO/PEDOT:PSS substrate with 3 wt% precursor solutions and PCPDTBT-PCBM BHJ film

Figure 1.6 *J-V* curves under AM 1.5 irradiation (100mW·cm$^{-2}$) of TBHJ hybrid solar cell devices fabricated under optimized processing condition with PCPDTBT-PC$_{61}$BM (1:3.6) BHJ film without DIO additive on $MAPbI_3$ nano dots (3 wt%) and DIO treated nano dots (3 wt%).

Figure 1.7 *J-V* curves under AM 1.5 irradiation (100mW·cm$^{-2}$) of TBHJ hybrid solar cell devices fabricated under optimized processing condition with PCPDTBT-PC$_{61}$BM(1:3.6) BHJ film with DIO additive (2vol%) on $PbI_2$ (3wt%).

Figure 1.8 (a) *J-V* curves under AM 1.5 irradiation (100mW·cm$^{-2}$) and (b) EQE spectra of TBHJ hybrid solar cell devices fabricated under optimized processing condition with $MAPbI_3$ nano dots and DIO treated nano dots on PCPDTBT-PC$_{61}$BM (1:3.6) BHJ film with DIO additive (2 vol%).

Figure 1.9 Transmittance spectra of $MAPbI_3$ nano dots (3 wt%), PCPDTBT-PC$_{61}$BM (1:3.6) BHJ film with DIO additive (2 vol%), and PCPDTBT-PC$_{61}$BM (1:3.6) BHJ film with DIO additive (2 vol%) on $MAPbI_3$ nano dots (3 wt%).

Figure 1.10 XRD patterns of $MAPbI_3$ nano dots (3 wt%) cast on ITO/PEDOT:PSS substrate before/after DIO pretreatment.

Figure 1.11 FESEM images of TBHJ hybrid films fabricated with (a) $MAPbI_3$ nano dots and (b) DIO treated nano dots on PCPDTBT-PC$_{61}$BM (1:3.6) BHJ film without DIO additive.

Figure 1.12 AFM (a, c, e) and FESEM (b, d, f) surface morphologies of PCPDTBT-PCBM (1:3.6) BHJ films with DIO additive (2 vol%) cast on ITO/PEDOT:PSS ((a, b) without the $MAPbI_3$ perovskite nano dots (3 wt%) (c,d) with the $MAPbI_3$ perovskite nano dots

(3 wt%), and (e, f) with the DIO treated $MAPbI_3$ nano dots (3 wt%)).

Figure 1.13 (a) SEM image for cross-sectioning "slice' of the TBHJ hybrid solar cell device using the FIB technique and cross-sectional (b) FESEM and (c) HRTEM images for this TBHJ solar cell configuration.

Figure 1.14 (a) *J-V* curves and (b) EQE spectra of TBHJ devices fabricated with the $MAPbI_3$ perovskite nano dots (3 wt%) and the DIO treated $MAPbI_3$ nano dots (3 wt%) on PCPDTBT-$PC_{71}BM$ (1:3.6) BHJ film with DIO additive (2 vol%) and compared to those of BHJ device without the $MAPbI_3$ perovskite nano dots (3 wt%).

Figure 2.1 Schematic descriptions for fabrication of solution-processed BHJ OSCs and PHJ PrSCs device structures with Si NC HEMs.

Figure 2.2 (a) HRTEM images (inset) of synthesized Si NCs (~5nm) and ultraviolet photoelectron spectra of p-type Si NCs and undoped Si NCs and (b) HOMO energy levels of these Si NCs, PTB7-Th, and $MAPbI_3$ materials.

Figure 2.3 The UPS spectra of (a) PTB7-Th and (b) $MAPbI_3$ materials, which were estimated from the ionization potentials.

Figure 2.4 DLS spectra of Si NCs prepared using a modified electrochemical etching method.

Figure 2.5 Photoluminescence spectra of p-Si NCs and undoped Si NCs, which were obtained from B-doped and undoped polycrystalline silicon wafers, respectively, by a modified electrochemical etching approach.

Figure 2.6 FESEM surface images of Si NCs spin-cast on the ITO/PEDOT:PSS substrates for various Si NCs concentrations ((a) 0, (b) 0.024, (c) 0.034, (d) 0.057, (e) 0.171, and (f) 0.854 mg/ml) in CB.

Figure 2.7 Photovoltaic performances of these BHJ OSC (black) and PHJ PrSC (red) devices with PEDOT:PSS/p-Si NC HEM layers fabricated at various concentrations (0, 0.024, 0.034, 0.057, 0.171, and 0.854 mg/ml) of Si NCs in CB solvent.

Figure 2.8 (a) Distribution *J-V* curves under AM 1.5 irradiation (100 $mW \cdot cm^{-2}$) for (a) BHJ OSCs and (b) PHJ PrSCs fabricated under optimized processing conditions with (p-type (red) and undoped (blue)) Si NCs (0.034mg/ml) deposited on PEDOT:PSS substrate and compared those (black) without Si NCs.

Figure 2.9 SCLC *J-V* characteristics obtained in the dark for hole-only devices, ITO/PEDOT:PSS/Si NCs/PTB7-Th:$PC_{71}BM$/Au and (b) EQE spectra of BHJ OSCs fabricated with/without Si NCs under optimized processing conditions.

# ABSTRACT

## 유기-무기 하이브리드 삼중접합 나노구조를 통한 유기태양전지 효율향상에 관한 연구

Jeong Hanbin
Advisor : Prof. Lee Jae Kwan, Ph.D.
Department of Carbon materials
Graduate School of Chosun University

태양전지는 크게 다결정 실리콘(silicon, Si)을 사용한 1세대 태양전지와 비정질 실리콘 및 1세대 태양전지는 단결정 및 $CdSe$, $CuInSe_2$ 를 사용한 2세대 태양전지와 유기물질을 사용한 3세대 태양전지로 구분할 수 있다.

3세대 태양전지는 염료감응태양전지, 양자점 태양전지 및 유기태양전지 등으로 나눌 수 있으며, 그 중에서 유기 태양전지는 1세대 태양전지에 비하여 생산단가를 기적으로 줄일 수 있는 기술로 1. 제조공정이 간편하고 2. 가벼우며, 3. 구부릴 수 있고 4. 디자인이 가능한 장점이 있으나 광전변환효율과 안정성이 비교적 낮은 점이 단점으로 지적되고 있다.

이러한 단점을 해결하기 위해 전도성과 안정성이 우수한 무기반도체 재료를 도입한 하이브리드 유기태양전지에 관한 연구가 진행되어 왔다. 하지만 유기물과 무기물의 경계면에서 여러 문제점이 나타나 유기태양전지의 문제점 극복에 한계점이 있어왔다.

이에 본 연구에서는 기존 벌크-헤테로 접합 구조의 태양전지에 새로운 무기물을 도입함으로써 세 가지 물질이 삼중접합 벌크-헤테로 접합 구조(ternary bulk heterojunction)를 가지게 하는 유기태양전지를 제작하였으며, 이를 통해 광전변환효율을 향상시키는 연구를 진행하였다.

먼저 최근 각광받고 있는 흡광영역이 넓고 exciton diffusion length와 electron and hole lifetime이 긴 페로브스카이트(perovskite)를 도입해 삼중접합

벌크-헤테로 접합구조의 유기태양전지를 제작했으며, 전하와 정공이 이동할 수 있는 활로를 추가적으로 열어준 결과 기존대비 약 28% 향상된 광전변환 효율을 확인할 수 있었다.

다음으로 도핑되지 않은 실리콘 nanocrystal과 p-type으로 도핑된 실리콘 nanocrystal을 도입해 삼중접합 구조의 유기태양전지를 제작하였으며, 이때 도입한 실리콘 nanocrystal이 hole extraction material로 작용함으로서 결정성 고분자의 정공이동도(hole mobility, $\mu_h$)를 향상시켜 기존대비 ~11% 와 ~23% 향상된 광전변환효율을 확인할 수 있었다.

Keywords: Solution-processing, Ternary bulk heterojunction, Silicon nanocrystals, Hole-extracting, Organic solar cells, Perovskite solar cells.

# Chapter 1.

# Organic-Inorganic Hybrid Ternary Bulk Hetero -junction of Nanostructured Perovskite-Low Bandgap Polymer-PCBM for Improved Efficiency of Organic Solar Cells

# A. Introduction

Solution-processed solar cells have been of great interest because of their facile and inexpensive manufacturing processes, including versatile methods such as inkjet, doctor-blade, and roll-to-roll printing.[1-2] Recently, considerable efforts have been focused on achieving competitive power conversion efficiencies (PCE) versus conventional silicon-based solar cells. As promising alternatives, solution-processed organic solar cells (OSCs) have exhibited excellent PCEs of up to 9.2% for low-bandgap thieno[3,4-*b*]thiopheneandbenzodithiophene (poly(thieno [3,4-*b*]thiophene -*alt*-benzodithiophene) semiconducting polymer series and [6,6] -phenyl-$C_{(61or71)}$-butyric acidmethylester ($PC_{(61or71)}BM$) bulk-heterojunctions (BHJs) with processing additives.[3] Various strategies have been adopted in order to obtain high PCE, for example, the development of high-performance semiconducting materials, including low-band gap π -conjugated polymer donors and fullerene derivative acceptors; effective functions with surface plasmon resonance, charge transport, optical spacing, and buffering in device structures; and morphological engineering of photosensitive films by post heat treatment, drying of casting solutions, or processing additives.[4-8]

Recently, solution-processable organometal halide perovskite solar cells have received considerable attention in the scientific community because they have exhibited breakthrough PCEs of over 15%.[9-13] These organometal halides, especially alkylammonium lead halides, $(RNH_3)PbX_3$ (R = alkyl, X = Cl, Br, I), are direct bandgap materials with hybrid organic-inorganic perovskite structures, which exhibit outstanding performance as electron and hole conductors as well as photosensitizers.[14-17] Notably, both the electron and hole diffusion lengths were determined on long-ranged scales of ~100 nm and above 1 μm in triiodide $(CH_3NH_3)PbI_3$ ($MAPbI_3$) and mixed halide $(CH_3NH_3)PbI_{3-x}Cl_x$ perovskite materials, respectively.[18-19] These perovskite solar cells are often fabricated using planar heterojunction (PHJ) bilayer structures of perovskite materials and 2,2',7,7' -tetrakis(N,N-di-*p*-methoxyphenylamine)-9,9'-spirobifluorene (spiro-MeOTAD) hole -transporting material (or PCBM electron-transporting material).[20-24] In particular, because the crystallinity, uniformity, and coverage of perovskite materials on the

substrate are critical issues improving the PCEs of devices, there has been extensive research on developing efficient methods for the fabrication of perovskite material layers.[11] We have also reported high-efficiency hybrid solar cells with well-organized $MAPbI_3$ perovskite (which were fabricated under various solution processing conditions) and $PC_{71}BM$ PHJ films.[25] Very recently, several research groups reported high PCEs in PHJ hybrid solar cell device structures composed of semiconducting donor/PCBM BHJ layers integrated on $(CH_3NH_3)PbI_{3-x}Cl_x$ perovskite material or a bilayer of $MAPbI_3$ perovskite/PCBM BHJ and a PCBM layer.[26-27] The use of the BHJ configuration in these device structures led to significant improvment in the PCEs compared with the conventional PHJ configurations in perovskite solar cells.

In contrast, we speculated that perovskite materials may be used to improve the performances of BHJ OSCs. Interestingly, we observed that the morphology of $MAPbI_3$ perovskite films was significantly affected by cast solvents, showing sparse surface coverage with overall longitudinal- and omni-directional constructive morphologies in dimethylformamide (DMF) and γ-butyrolacton, respectively on indium tin oxide (ITO)/poly(3,4-ethylenedioxythiophene):poly(styrenesulfonate) (PEDOT:PSS) substrates.[25] Thus, we have attempted to fill the polymer/PCBM BHJ composite into the sparse coverage of $MAPbI_3$ perovskite on ITO/PEDOT:PSS substrates to induce a multi-BHJ system consisting of $MAPbI_3$ perovskite/polymer/PCBM, which might be composed of polymer-PCBM, perovskite-polymer, perovskite-PCBM, or polymer-perovskite-PCBM. Herein, we report the improved efficiency in OSCs fabricated from the low-bandgap poly[2,6-(4,4-bis-(2-ethylhexyl)-4*H*-cyclopenta [2,1-*b*;3,4-*b*′]dithiophene)-*alt*-4,7(2,1,3-benzothiadiazole)] (PCPDTBT)-PCBM BHJ with 1,8-diiodooctane (DIO) processing additive[8] by incorporating $MAPbI_3$ perovskite, introducing new perovskite-polymer-PCBM ternary bulk heterojunction (TBHJ) hybrid solar cells. The sparse coverage of the $MAPbI_3$ perovskite on the ITO/PEDOT:PSS substrate was readily demonstrated by varying the concentration of the $MAPbI_3$ perovskite precursor in the DMF solvent, in which the $MAPbI_3$ nano dots were particularly observed at low concentrations below 7 wt% without perovskite crystal structures.

Notably, outstanding performances were observed for the TBHJ hybrid device configuration of ITO/PEDOT:PSS/$MAPbI_3$-PCPDTBT-PCBM/Al fabricated from the BHJ system with DIO additive, which played a key role in developing perovskite structures of $MAPbI_3$ nano dots[28] and induced (110) directional crystallinity growth of the longitudinal constructive morphologies like nano rods, showing ~28% enhanced PCE compared with that of the PCPDTBT-PCBM BHJ. Figure 1.1 shows the (a) preparation of nanostructured $MAPbI_3$-PCPDTBT-PCBM TBHJ film on ITO/PEDOT:PSS substrate, (b) TBHJ hybrid solar cell device structure, and © charge transfers in simplified TBHJ interfaces of (1) PCPDTBT-PCBM, (2) PCBM-$MAPbI_3$ -PCPDTBT, (3) $MAPbI_3$-PCBM. The $MAPbI_3$-PCPDTBT-PCBM TBHJ configuration might have afforded these device structures with high PCEs from charge transfers occurring in multi BHJs of PCPDTBT-PCBM, $MAPbI_3$-PCPDTBT, and $MAPbI_3$-PCBM.

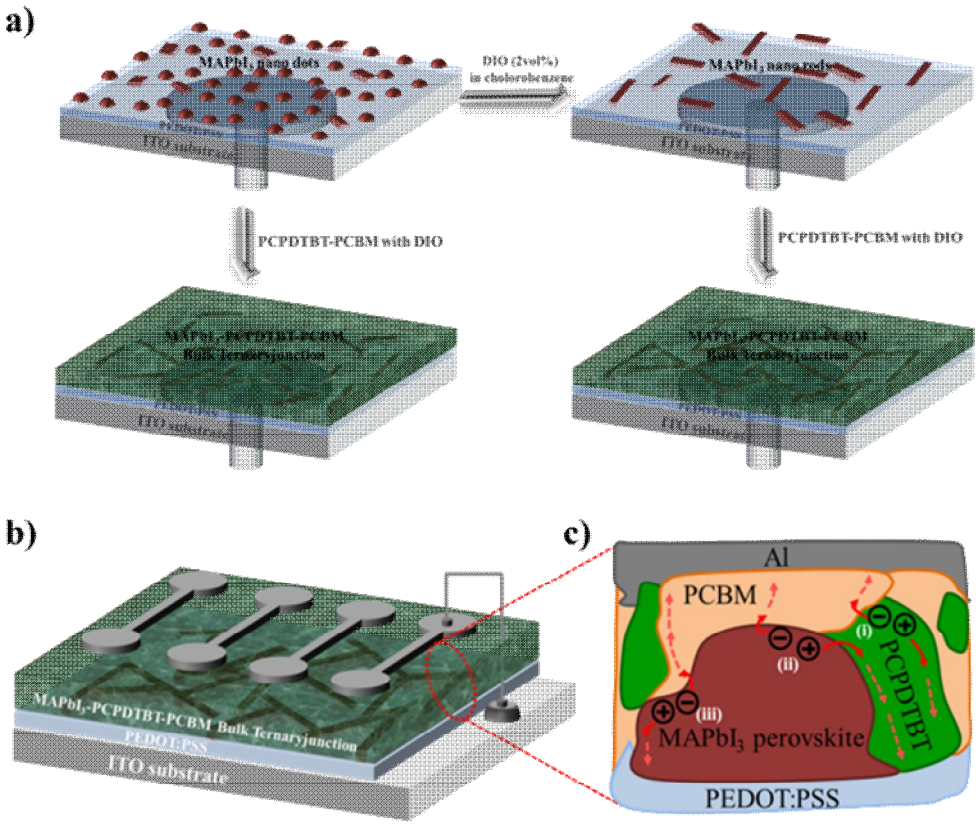


***Figure 1.1.*** Schematic descriptions for (a) preparation of nanostructured $MAPbI_3$-PCPDTBT-PCBM TBHJ film on ITO/PEDOT:PSS substrate, (b) TBHJ hybrid solar cell device structure, and (c) charge transfers in simplified TBHJ interfaces of (1) PCPDTBT-PCBM, (2) PCBM-$MAPbI_3$-PCPDTBT, and (3) $MAPbI_3$-PCBM.

# B. Experimental methods

## 1. Materials

$PbI_2$ was purchased from Aldrich and $CH_3NH_3I$ was prepared according to the method reported previously.[20] All solvents were purchased from Sigma-Aldrich, TCI, and Alfa Aesar and were purified using appropriate methods. The $MAPbI_3$ precursor solution was prepared under a nitrogen atmosphere. The PCPDTBT and PCBM were obtained from 1-Material and Nano-C, respectively.

## 2. Measurements and instruments

The transmittance spectra were recorded on a Perkin-Elmer Lambda 2S ultraviolet (UV)-visible spectrometer. The surface morphologies were imaged using atomic force microscopy (AFM, Park NX10, Park System, Korea), field emission scanning electron microscope (FESEM, Nova nanoSEM 450, FEI, Netherlands), and high-resolution transmission electron microscopy (HRTEM, G2 F20, FEI Tecnai, Netherlands). The perovskite crystallinities of the $MAPbI_3$ nano dots were investigated using X-ray diffraction (XRD, D/Max2500 V/PC, Rigaku Corp, Japan). The solar cells efficiencies were characterized under simulated 100 $mW{\cdot}cm^{-2}$ AM 1.5G irradiation from a Xe arc lamp with an AM 1.5 global filter. The simulator irradiance was characterized using a calibrated spectrometer and the illumination intensity was set using a silicon diode with an integrated KG1 optical filter certified by the National Renewable Energy Laboratory (NREL). The spectral mismatch factors were calculated to be less than 5% for each device. The short circuit currents were also found to be within 5% of the values calculated using the integrated external quantum efficiency (EQE) spectra and the solar spectrum. The applied potential and cell currents were measured using a Keithley model 2400 digital source meter. The current ($J$)-voltage ($V$) curves were measured at a voltage settling time of 100 ms. The EQEs were measured

by under filling the device area using a reflective microscope objective to focus the light output from a 75 W Xe lamp, monochromator, and optical chopper; the photocurrent was measured using a lock-in amplifier; the absolute photon flux was determined using a calibrated silicon photodiode and was recorded for five seconds per point (80 points) from 350-1100 nm.

## 3. Device fabrication

BHJ films with PCPDTBT－PCBM were prepared under optimized conditions according to reported protocol.[8] The ITO-coated glass substrates were cleaned with detergent, ultrasonicated in acetone and isopropyl alcohol, and then dried overnight in an oven. PEDOT:PSS (Heraeus, Clevios P VP.AI 4083) in an aqueous solution was spin-cast on the ITO substrates to form a film of thickness ~35 nm. The substrate was dried for 10 min at 140 ℃ in air before being transferred into a glovebox for spin-casting of the $MAPbI_3$ precursor solution and the photoactive layer. The $MAPbI_3$ precursor solution was prepared using $PbI_2$ and $CH_3NH_3I$ (molar ratio, 1:1) in DMF at 1, 3, 5, 7, and 10 wt % and stirred at 60 ℃ for 12h. The $MAPbI_3$ precursor solution was spin-cast on the PEDOT:PSS/ITO substrate in two consecutive steps at 2000 and 5000 rpm for 30 and 20 s, respectively. Then, the substrate was dried on a hot plate at 100 ℃ for 10 min. The DIO treated $MAPbI_3$ nano dots were spin-cast with the DIO solution (2 vol % in chlorobenzene) at 2000 rpm for 60s, followed by heat-treatment at 60 ℃ for 10 min. The PCPDTBT－PCBM BHJ blend solution (weight ratio, 1:3.6) solutions were spincast on top of the $MAPbI_3$ layer followed by heat-treatment at 80 ℃ for 10 min. Finally, an Al metal electrode of thickness ~100 nm was deposited on top of the $MAPbI_3$－PCPDTBT－PCBM TBHJ film under reduced pressure (less than $10^{-6}$ Torr).

## C. Result and discussion

Figure 1.2 presents FESEM surface images of $MAPbI_3$ materials that were fabricated by varying the concentration (1, 3, 5, 7, and 10 wt %) of the $MAPbI_3$ perovskite precursor in the DMF solvent that was spin-cast on the ITO/PEDOT:PSS substrates. Figure 1.2 shows that the longitudinal constructive morphologies of the $MAPbI_3$ perovskite films cast from the 10 wt % precursor solution generally exhibited sparse surface coverage on the ITO/PEDOT:PSS substrate, whereas omni-directional morphologies such as nanodots with a grain size of 50−200 nm were mainly observed for concentrations below 7 wt %. These nano dots cast on ITO/PEDOT:PSS substrates exhibited sparse surface coverage and dense surface coverage in the 1−3 wt % and 5−7 wt % precursor solutions, respectively, and Pb atoms were not detected in the empty space (see Figure 1.3). We investigated the perovskite crystallinity of these materials through XRD analysis (Figure 1.4). Notably, the XRD patterns of these films presented heterogeneous crystallinities of $PbI_2$ without typical patterns of $MAPbI_3$ perovskite crystallinity.[10] A sharp XRD pattern for $MAPbI_3$ perovskite crystallinity was observed in precursor solutions with concentration greater than 10 wt %.

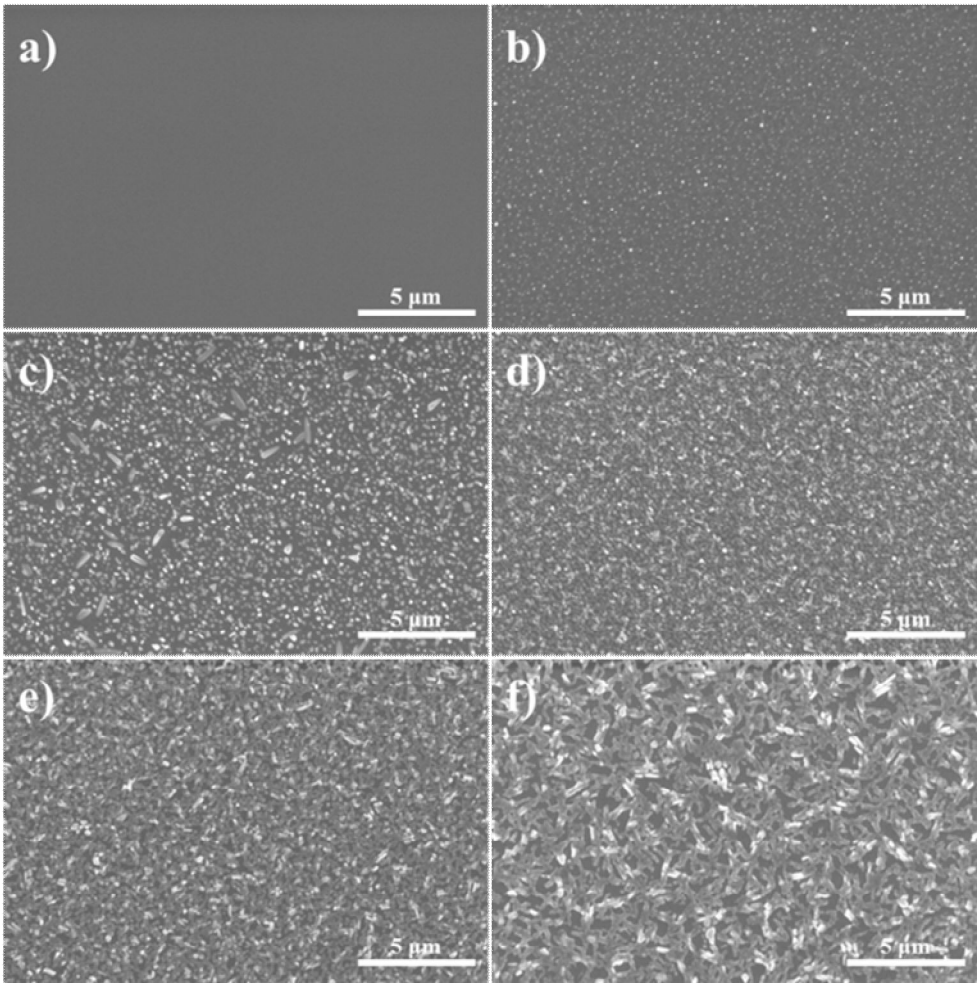


***Figure 1.2*** FESEM surface images of $MAPbI_3$ materials, which were fabricated by caring the concentration (a) 0, (b) 1, (c) 3, (d) 5, (e) 7, and (f) 10 wt% of $MAPbI_3$ perovskite precursor in DMF solvent, spin-cast on the ITO/PEDOT:PSS substrate.

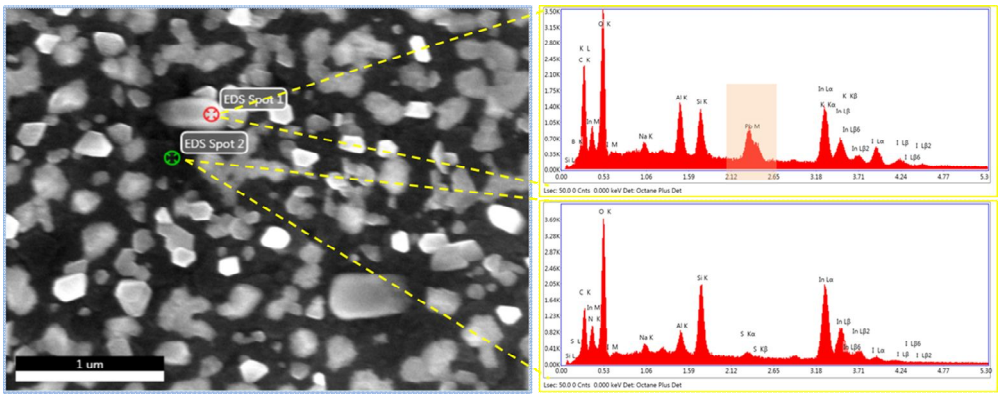


***Figure 1.3*** FESEM surface images and EDAX analysis of $MAPbI_3$ materials, which were fabricated by caring the concentration (3 wt%) of $MAPbI_3$ perovskite precursor in DMF solvent, spin-cast on the ITO/PEDOT:PSS substrate.

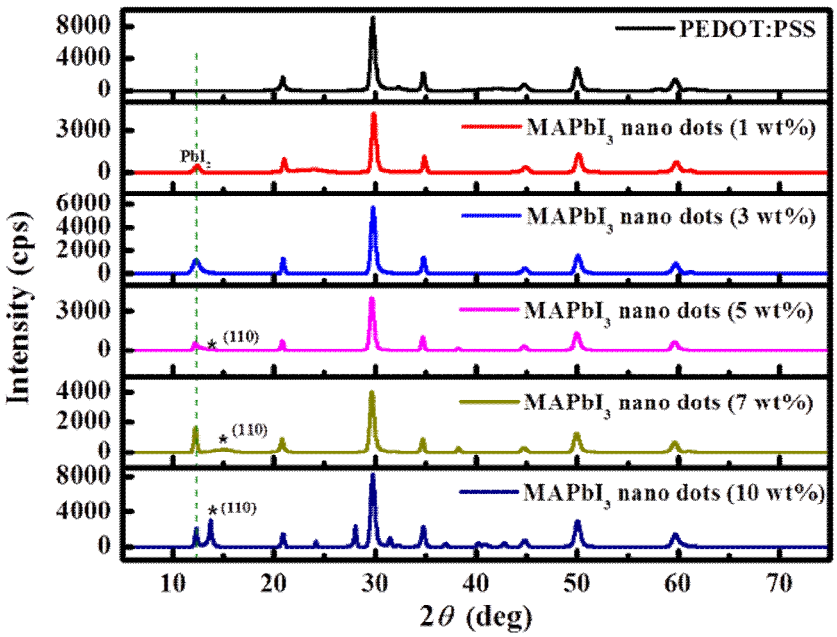


***Figure 1.4*** XRD patterns of $MAPbI_3$ materials, which were fabricated by caring the concentration (1, 3, 5, 7, and 10wt%) of $MAPbI_3$ perovskite precursor in DMF solvent, spin-cast on the ITO/PEDOT:PSS substrate.

Based on these results, we employed the aforementioned $MAPbI_3$ films in an OSC fabricated from the PCPDTBT－PCBM BHJ film with DIO additive. Figure 1.5 shows (a) the photovoltaic performances of the TBHJ hybrid solar cell devices fabricated using $MAPbI_3$ perovskite precursors of various concentrations (1, 3, 5, 7, and 10 wt %) in DMF solvent compared with that without $MAPbI_3$ materials, and (b) the XRD patterns of the $MAPbI_3$ nano dots cast on a ITO/PEDOT:PSS substrate with 3 wt % precursor solution and the PCPDTBT－PCBM BHJ film with DIO additive on these $MAPbI_3$ nanodots.

These values were determined from the average of individual TBHJ hybrid solar cells fabricated under conditions optimized from OSCs without $MAPbI_3$ materials. As shown in Figure 1.5.a, the TBHJ devices fabricated with 3 wt % precursor solutions exhibited improved photovoltaic performance compared to those without $MAPbI_3$. However, the TBHJ devices fabricated with higher precursor solutions than 5 wt % exhibited some dismal photovoltaic performances. These results indicate that the dense surface coverage of noncrystalline $MAPbI_3$ might be an obstacle to charge transfer from PCPDTBT to PEDOT:PSS. Interestingly, the (110) directional crystallinity of $MAPbI_3$ perovskite was observed in the XRD pattern of the PCPDTBT－PCBM BHJ film with DIO additive cast on these ITO/PEDOT:PSS/$MAPbI_3$ nano dots (Figure 1.5.b). In addition, the TBHJ hybrid solar cell devices fabricated from the PCPDTBT－PCBM BHJ film (without DIO additive) cast on these ITO/PEDOT:PSS/$MAPbI_3$ nano dots (3 wt %) did not exhibit improved photovoltaic performance compared to those with DIO additive Figure 1.6). Besides, the TBHJ devices fabricated with $PbI_2$ (3 wt %) solutions (without MAI) exhibited worse efficiency than those with $MAPbI_3$ (3 wt %) precursor solutions (Figure 1.7). These results show that the DIO processing additive could lead to the development of the perovskite structures of $MAPbI_3$ nano dots,[28] which result in improved photovoltaic performance of the TBHJ hybrid solar cells.

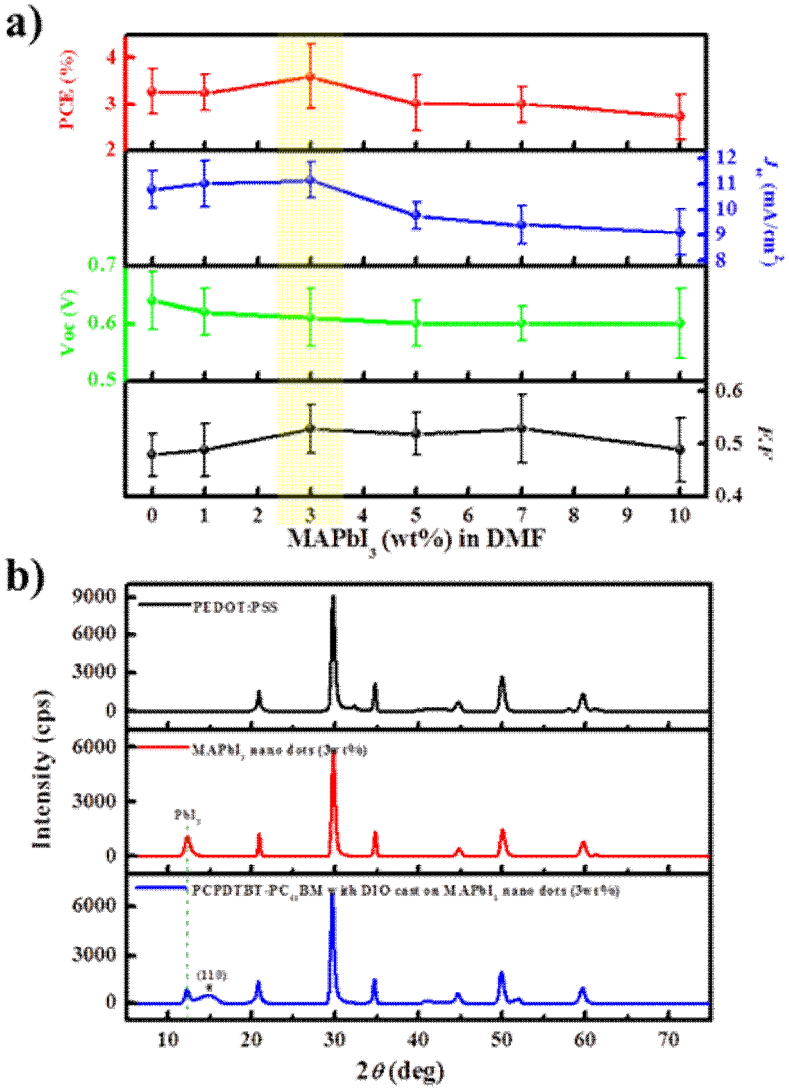


***Figure 1.5*** (a) Photovoltaic performances of TBHJ hybrid solar cell devices fabricated from PCPDTBT-PCBM BHJ film with DIO additive using $MAPbI_3$ perovskite precursor of the various concentration (0, 1, 3, 5, 7, and 10 wt%) in DMF solvent and (b) XRD patterns of $MAPbI_3$ nano dots cast on ITO/PEDOT:PSS substrate with 3wt% precursor solutions and PCPDTBT-PCBM BHJ film with DIO additive on these $MAPbI_3$ nanodots.

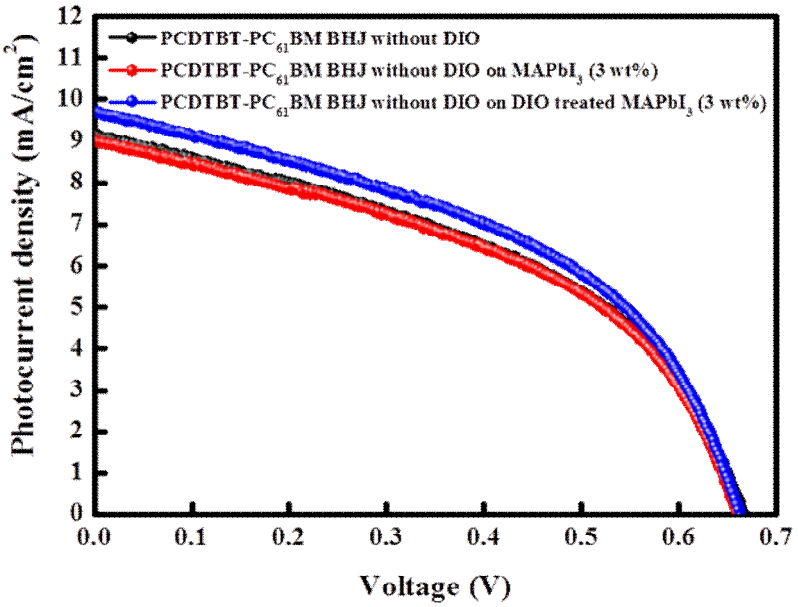


***Figure 1.6*** *J-V* curves under AM 1.5 irradiation (100mW·cm$^{-2}$) of TBHJ hybrid solar cell devices fabricated under optimized processing condition with PCPDTBT-$PC_{61}$BM (1:3.6) BHJ film without DIO additive on $MAPbI_3$ nano dots (3 wt%) and DIO treated nano dots (3 wt%).

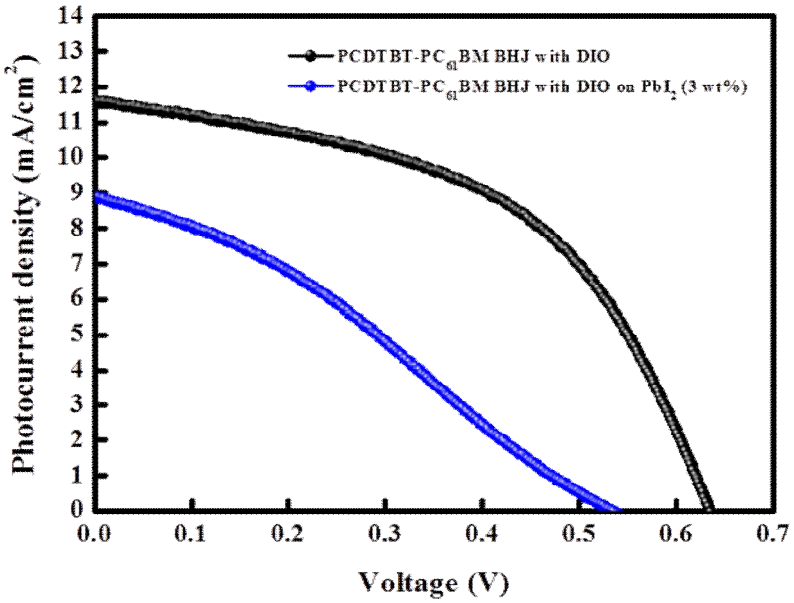


***Figure 1.7*** *J-V* curves under AM 1.5 irradiation (100mW·cm$^{-2}$) of TBHJ hybrid solar cell devices fabricated under optimized processing condition with PCPDTBT-$PC_{61}BM$(1:3.6) BHJ film with DIO additive (2vol%) on $PbI_2$ (3wt%).

To clarify the DIO efficacy, we prepared $MAPbI_3$ perovskite nano dots (3 wt %) treated with DIO (2 vol %) in chlorobenzene. Figure 1.8 presents the $J-V$ curves under AM 1.5 irradiation (100 $mWcm^{-2}$) and the EQE spectra for TBHJ hybrid solar cell devices fabricated under optimized processing conditions with these $MAPbI_3$ nano dots and PCPDTBT−PCBM (1:3.6) BHJ film with DIO additive (2 vol %). The corresponding values are summarized in Table 1. As shown in Figure 1.8.a and Table 1, the TBHJ devices fabricated with the $MAPbI_3$ perovskite nano dots and the DIO treated $MAPbI_3$ perovskite nano dots exhibited ~14% and ~28% enhanced PCEs (maximum/average) of 4.79/4.47% with a short-circuit current density ($J_{sc}$) of 13.9 $mA{\cdot}cm^{-2}$, open-circuit voltage ($V_{oc}$) of 0.63 V, and fill factor ($F.F$) of 0.55; and 4.24/4.05% with $J_{sc}$ = 13.0 $mA{\cdot}cm^{-2}$, $V_{oc}$ = 0.63 V, and $F.F$ = 0.52, respectively. These $J_{sc}$ and $F.F$ values are higher than those (PCE = 3.73/3.58% with $J_{sc}$ = 11.6 $mA{\cdot}cm^{-2}$, $V_{oc}$ = 0.64 V, and $F.F$ = 0.51) of the BHJ device without $MAPbI_3$ perovskite nano dots. As shown in Figure 1.8.b, these increased photocurrents may originate from the higher quantum efficiencies in the visible region, especially 400−800 nm, indicating that the photocurrent was contributed by the charge transfer from the $MAPbI_3$ perovskite nano dots to PCBM. Since the $MAPbI_3$ perovskite nano dots exhibited a spectral response in the light absorption region of 350−800 nm (Figure 1.9, the EQE spectra of these devices were closely correlated to the photocurrents in the $J-V$ curves. Moreover, these DIO treatment approaches enabled growth of the $MAPbI_3$ nano dots having longitudinal constructive morphologies such as nano rods with the (110) directional crystallinity, which exhibited further increased perovskite crystallinities (see Figures 1.10 and 1.11).

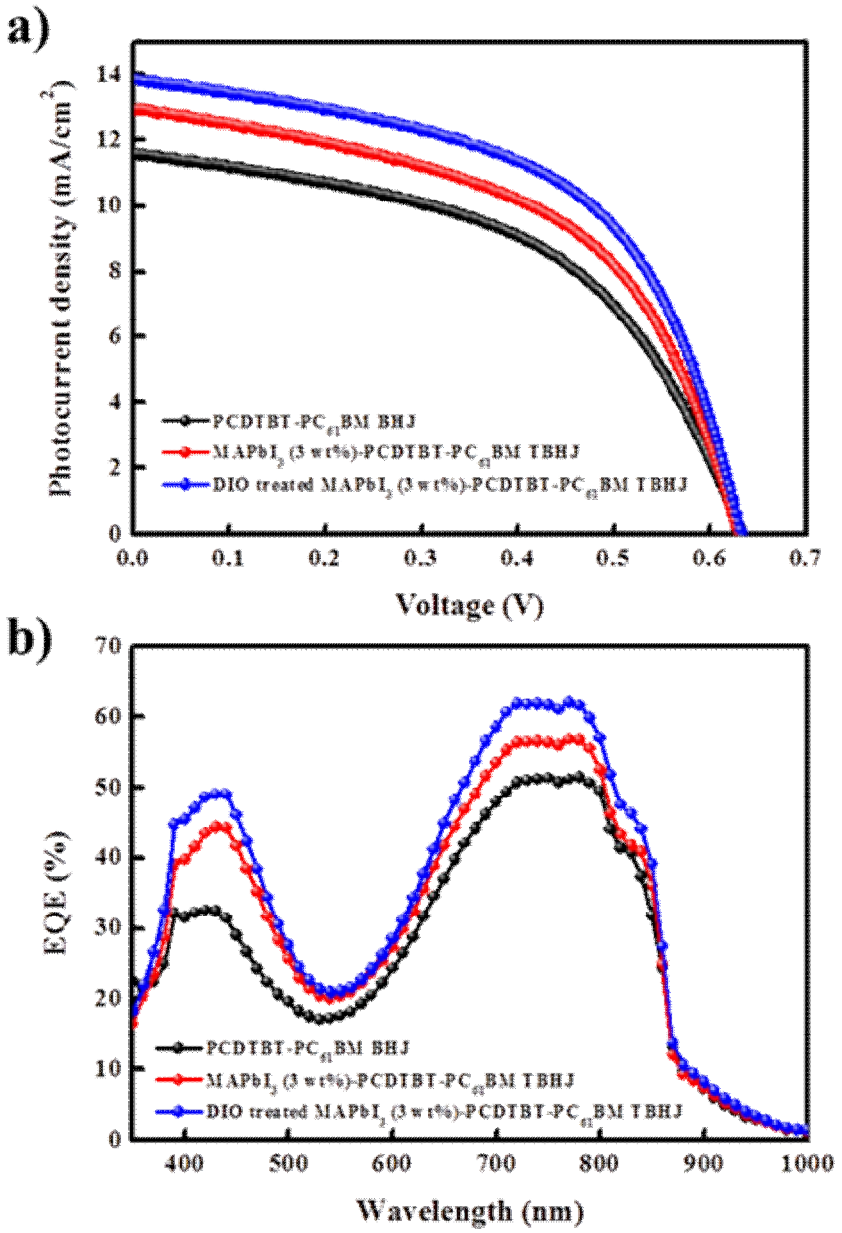


***Figure 1.8*** (a) *J-V* curves under AM 1.5 irradiation (100mW·cm$^{-2}$) and (b) EQE spectra of TBHJ hybrid solar cell devices fabricated under optimized processing condition with $MAPbI_3$ nano dots and DIO treated nano dots on PCPDTBT-$PC_{61}BM$ (1:3.6) BHJ film with DIO additive (2 vol%).

***Table 1.1*** Photovoltaic performances of solar cell devices fabricated with $MAPbI_3$ perovskite, PCPDTBT, and PCBM.[a]

| no. | $MAPbI_3$[b] | PCBM | $J_{sc}$ ($mAcm^{-2}$) | $V_{oc}$ (V) | *F.F* | $\eta$ max/ave (%) |
|---|---|---|---|---|---|---|
| 1 | none | $PC_{61}BM$ | 11.6 | 0.64 | 0.51 | 3.73/3.58 |
| 2 | none | $PC_{71}BM$ | 14.5 | 0.61 | 0.51 | 4.50/4.29 |
| 3 | nano dots | $PC_{61}BM$ | 13.0 | 0.63 | 0.52 | 4.24/4.05 |
| 4 | nano dots | $PC_{71}BM$ | 14.7 | 0.61 | 0.53 | 4.76/4.55 |
| 5 | DIO-treated nano dots | $PC_{61}BM$ | 13.9 | 0.63 | 0.55 | 4.79/4.47 |
| 6 | DIO-treated nano dots | $PC_{71}BM$ | 15.2 | 0.62 | 0.55 | 5.19/4.98 |

[a]The performances are determined under simulated 100 $mW \cdot cm^{-2}$ AM 1.5G illumination. The light intensity using calibrated standard silicon solar cells with a proactive window made from KG5 filter glass traced to the NREL. The masked active area of device is 4 $mm^2$. These values were determined from the average of individual 25 solar cells fabricated under each optimized conditions. [b]The optimized $MAPbI_3$ nano dots used in this study were prepared by $PbI_2$ and $CH_3NH_3I$ in DMF with 3 wt% and the DIO-pretreatment of $MAPbI_3$ nano dots were proceeded through spin-casting of the DIO solution (2 vol% in chlorobenzene).

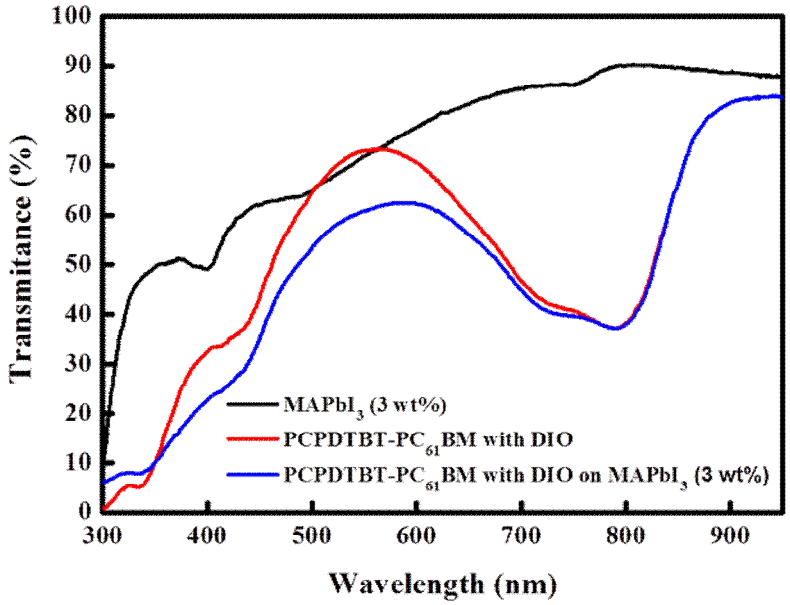


***Figure 1.9*** Transmittance spectra of $MAPbI_3$ nano dots (3 wt%), PCPDTBT-$PC_{61}$BM (1:3.6) BHJ film with DIO additive (2 vol%), and PCPDTBT-$PC_{61}$BM (1:3.6) BHJ film with DIO additive (2 vol%) on $MAPbI_3$ nano dots (3 wt%).

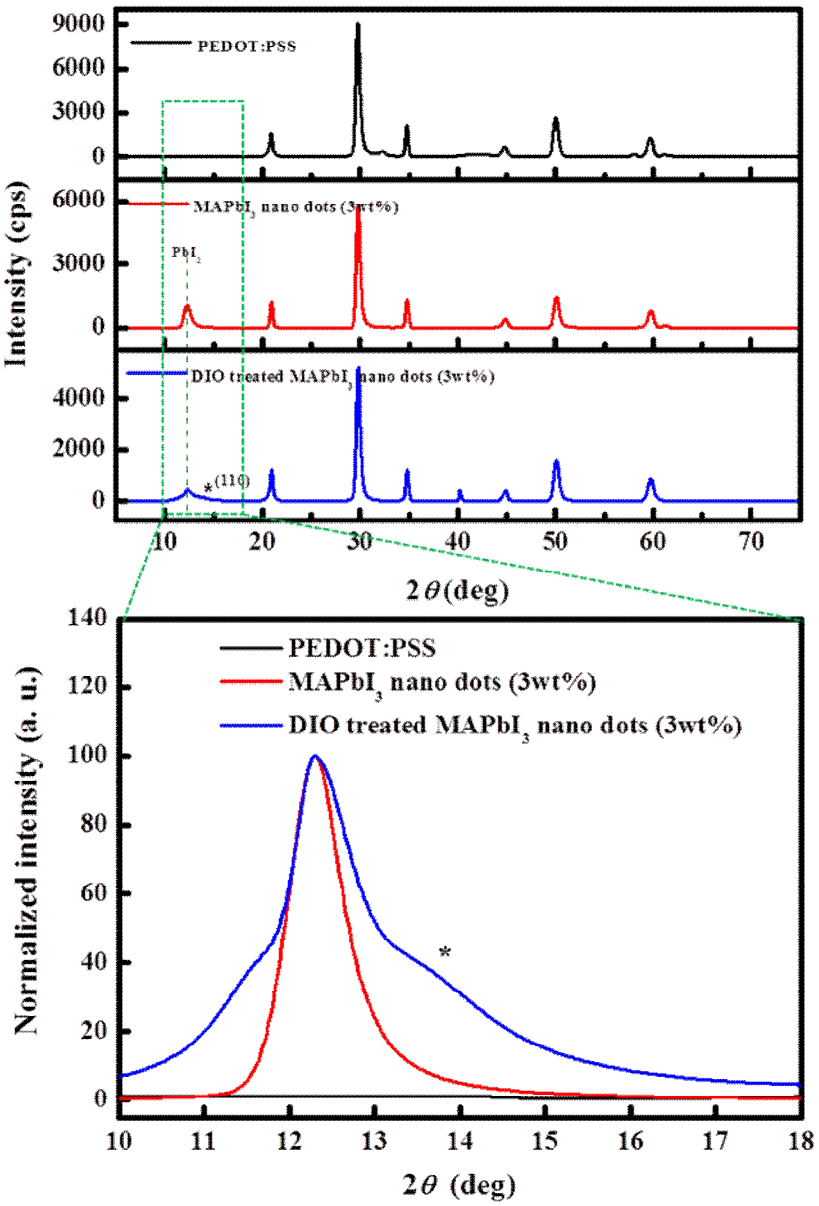


***Figure 1.10*** XRD patterns of $MAPbI_3$ nano-dots (3 wt%) cast on ITO/PEDOT:PSS substrate before/after DIO pretreatment.

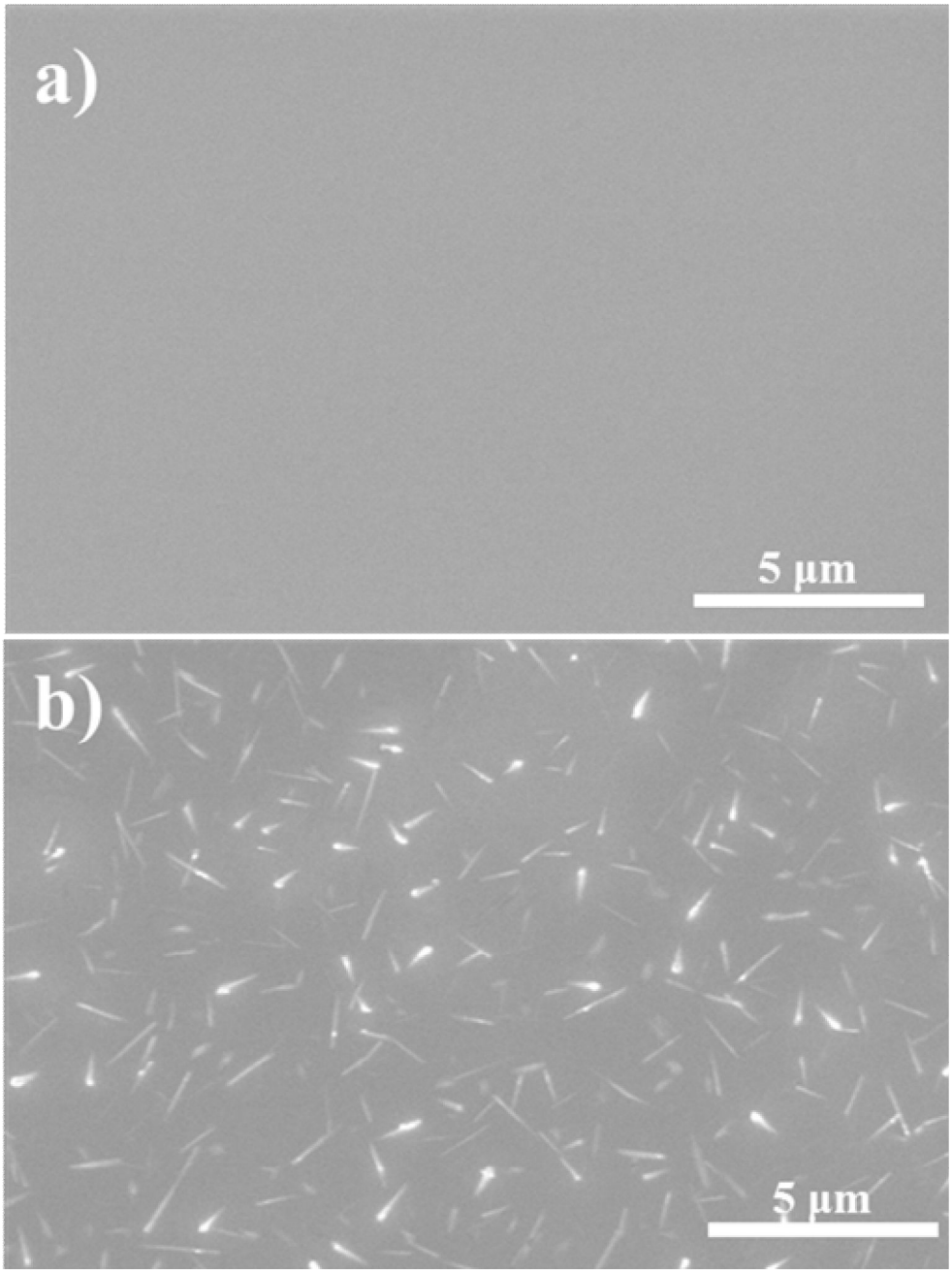


***Figure 1.11*** FESEM images of TBHJ hybrid films fabricated with (a) $MAPbI_3$ nano dots and (b) DIO treated nano dots on PCPDTBT-$PC_{61}BM$ (1:3.6) BHJ film without DIO additive.

Next, we characterized the surface and interface morphologies using AFM and FESEM analyses, respectively. Figure 1.12 shows the AFM (a, c, e) and FESEM (b, d, f) surface morphologies of the PCPDTBT－PCBM (1:3.6) BHJ films with DIO additive (2 vol %) cast on ITO/PEDOT:PSS ((a, b) without the MAPbI3 perovskite nano dots (3 wt %) (c, d) with the $MAPbI_3$ perovskite nano dots (3 wt %) and (e. f) with the DIO treated $MAPbI_3$ nano dots (3 wt %)). As shown in Figure 1.12, the spin-cast PCPDTBT－PCBM composite with DIO filled the large empty spaces in the sparse surface coverage of $MAPbI_3$ nano dots (3 wt %) on the ITO/PEDOT:PSS substrate, indicating that the surface morphologies of $MAPbI_3$ perovskite nano rods grew significantly owing to the DIO additives. These results are consistent with those observed in Figure 1.10.

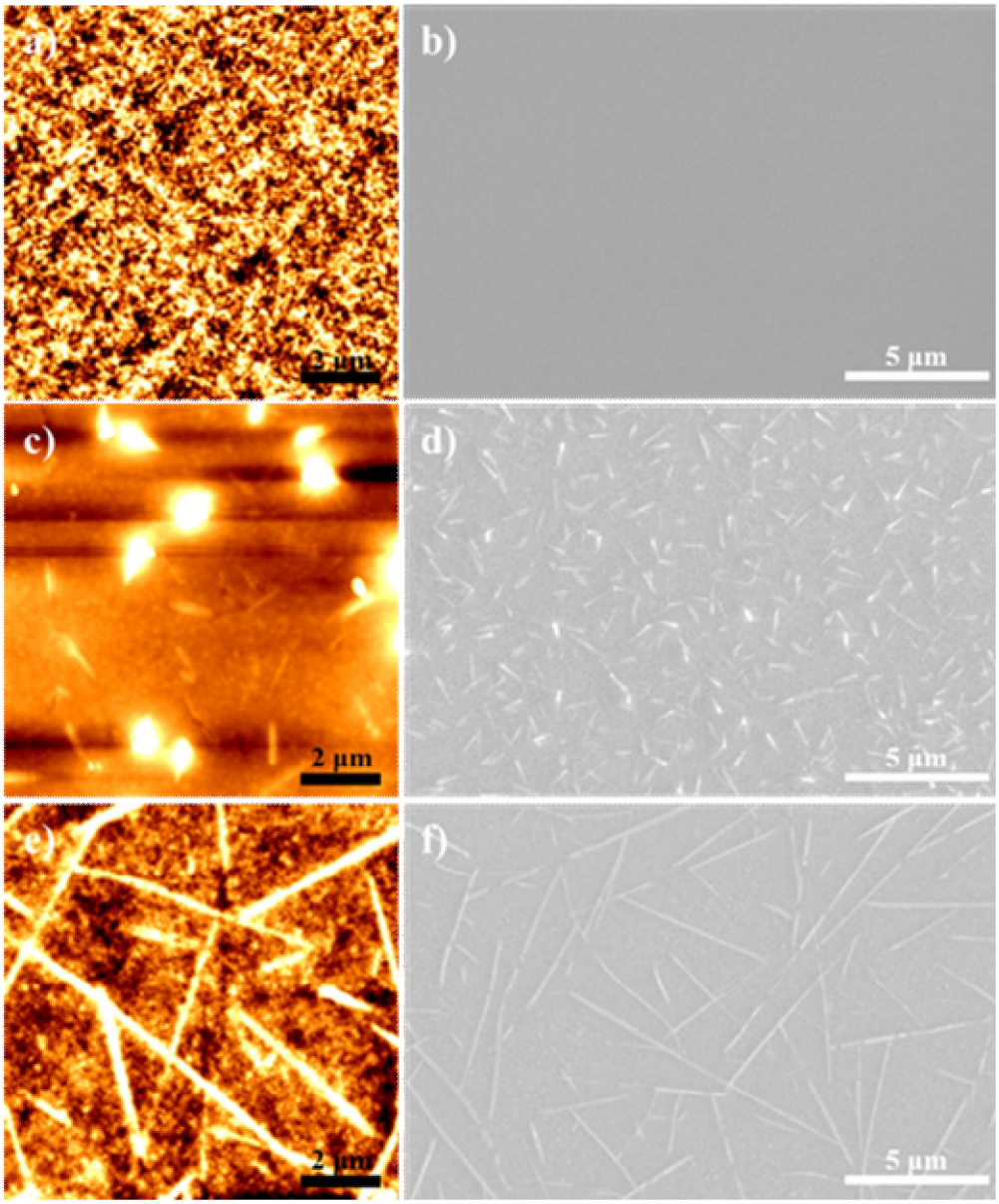


***Figure 1.12*** AFM (a, c, e) and FESEM (b, d, f) surface morphologies of PCPDTBT-PCBM (1:3.6) BHJ films with DIO additive (2 vol%) cast on ITO/PEDOT:PSS ((a, b) without the $MAPbI_3$ perovskite nano dots (3 wt%) (c,d) with the $MAPbI_3$ perovskite nano dots (3 wt%), and (e, f) with the DIO treated $MAPbI_3$ nano dots (3 wt%)).

We also prepared a thin section (slice) of ~100 nm in the TBHJ hybrid solar cell devices using the focused ion beam (FIB) technique to investigate the vertically formed morphologies and interfacial heterojunctions between nanostructured $MAPbI_3$ perovskite, PCPDTBT, and PCBM. Figure 1.13 shows the (a) FESEM image for the "slice" of TBHJ hybrid solar cell device using the FIB technique as well as the cross-sectional (b) FESEM and (c) HRTEM images for the "slice" of this TBHJ solar cell configuration. As shown in Figure 1.13, the TBHJ films were well organized without interfacial dead space, facilitating the exciton dissociation in the multi-BHJ system between the nanostructured $MAPbI_3$ perovskite, PCPDTBT, and PCBM, which might be composed of PCPDTBT－PCBM, $MAPbI_3$ perovskite－PCBM, or $MAPbI_3$ perovskite－PCPDTBT.

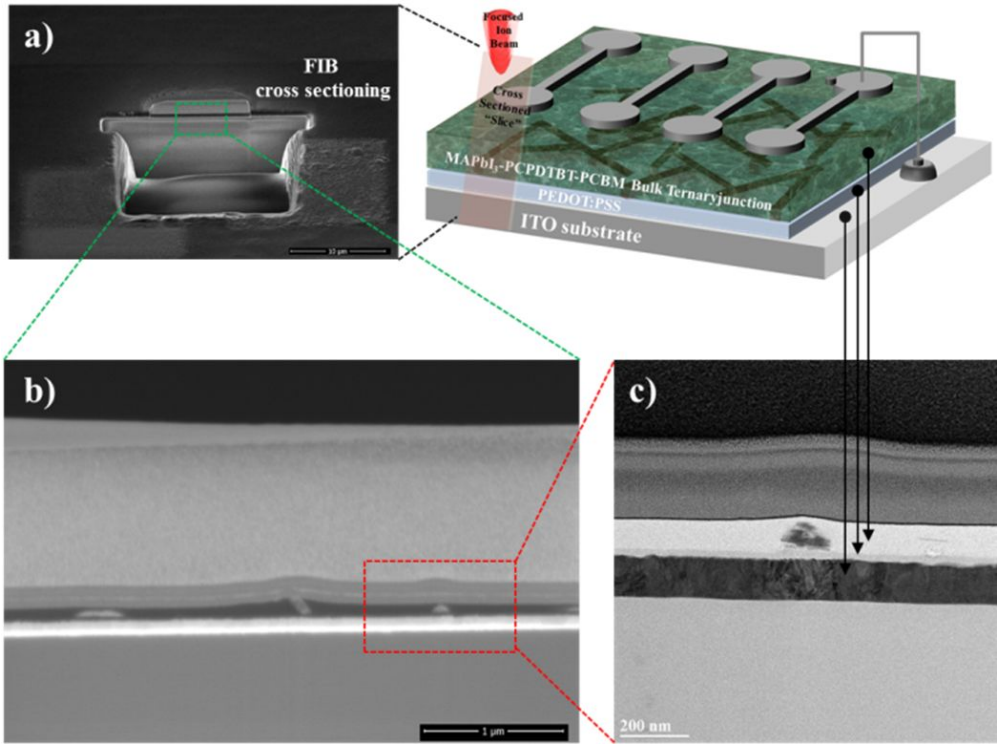


***Figure 1.13*** (a) SEM image for cross-sectioning "slice' of the TBHJ hybrid solar cell device using the FIB technique and cross-sectional (b) FESEM and (c) HRTEM images for this TBHJ solar cell configuration.

Figure 1.14 shows the (a) $J-V$ curves and (b) EQE spectra of TBHJ devices fabricated with the $MAPbI_3$ perovskite nano dots (3 wt %) and the DIO treated $MAPbI_3$ nano dots (3 wt %) and PCPDTBT−$PC_{71}BM$ (1:3.6) BHJ film with DIO additive (2 vol %) compared to those of the BHJ device without the $MAPbI_3$ perovskite nano dots (3 wt %). Apart from the slightly increased *F.F* values, the photovoltaic performance of the TBHJ devices fabricated with the $MAPbI_3$ perovskite nano dots and PCPDTBT−$PPC_{71}BM$ (1:3.6) BHJ film with DIO additive (2 vol %) was similar to that of the devices without the $MAPbI_3$ perovskite nano dots.

These results indicate that the photocurrent enhancement provided by the $MAPbI_3$ perovskite nano dots might be attenuated by the $PC_{71}BM$ because the spectral response of $PC_{71}BM$ overlaps well with the optical absorption of the $MAPbI_3$ perovskite nano dots in the visible region (Figure 1.14.b). The BHJ solar cell devices fabricated with polymer−.$PC_{71}BM$ composites often exhibited improved photovoltaic performance compared to those prepared with a polymer−$PC_{61}BM$ composite because $PC_{71}BM$ has a better spectral response than that of $PC_{61}BM$.[29] Nevertheless, the best PCEs (maximum/average) of 5.19/4.98% with a $J_{sc}$ of 15.2 $mA{\cdot}cm^{-2}$, $V_{oc}$ of 0.62 V, and *F.F* of 0.55 were obtained in the TBHJ devices fabricated with DIO treated $MAPbI_3$ nano dots (3 wt%), which is ~15% higher than those of BHJ device without $MAPbI_3$ perovskite nano dots (PCE = 4.50/4.29% with $J_{sc}$ = 14.5 $mA{\cdot}cm^{-2}$, $V_{oc}$ = 0.61 V, and *F.F* = 0.51). As shown in Figure 1.14.b, these increased photocurrents should be dominated from the higher quantum efficiencies in the absorption region of 400− 650 nm even though the EQE spectra of the TBHJ devices composed of $MAPbI_3$ perovskite−PCPDTBT−$PC_{71}BM$ exhibited lower values at 650−800 nm compared to the BHJ device without $MAPbI_3$ nano dots. These results indicate

that the TBHJ hybrid solar cells comprised of $MAPbI_3$ perovskite nano dots-low bandgap polymer－PCBM might be new alternatives to improve the photovoltaic performance of solar cell devices with the BHJ configuration of low bandgap polymer－PCBM.

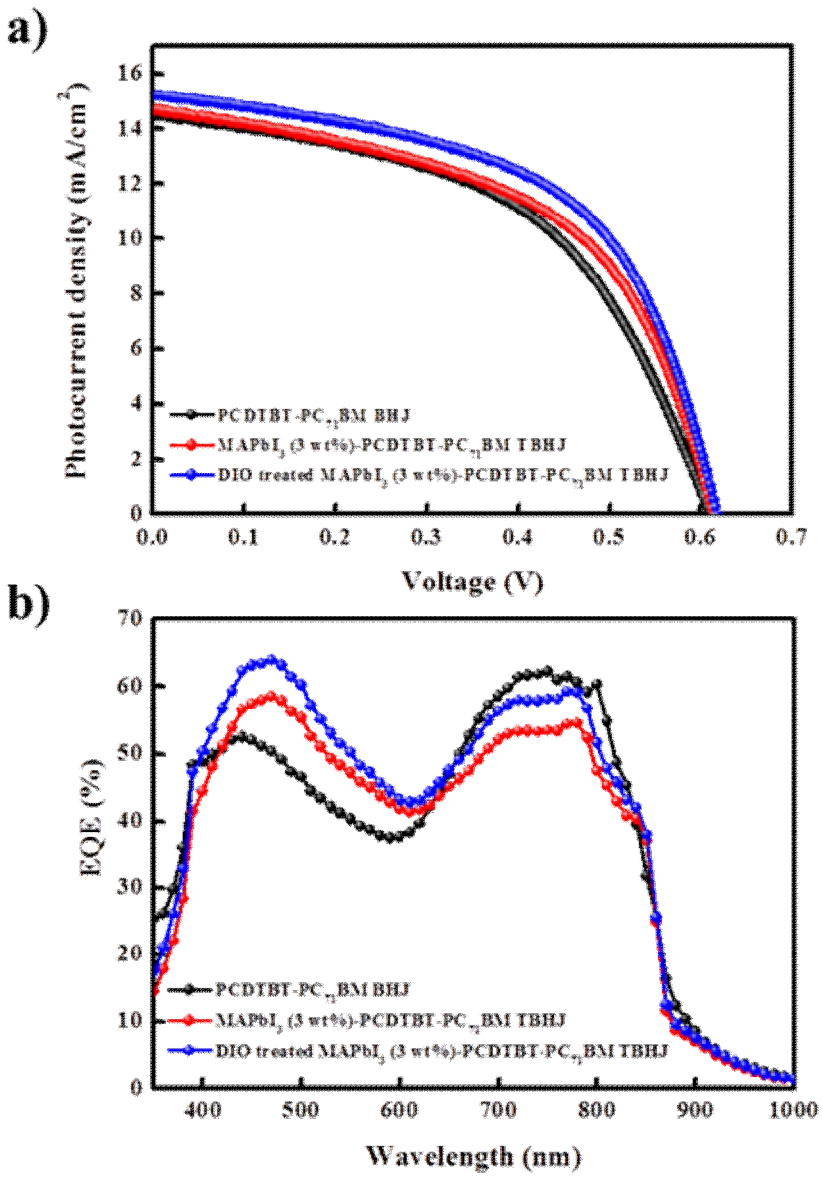


***Figure 1.14*** (a) *J-V* curves and (b) EQE spectra of TBHJ devices fabricated with the $MAPbI_3$ perovskite nano dots (3 wt%) and the DIO treated $MAPbI_3$ nano dots (3 wt%) on PCPDTBT-$PC_{71}BM$ (1:3.6) BHJ film with DIO additive (2 vol%) and compared to those of BHJ device without the $MAPbI_3$ perovskite nano dots (3 wt%).

## D. Conclusion

We have demonstrated high-performance TBHJ hybrid solar cells composed of nanostructured $MAPbI_3$ perovskite－PCPDTBT－PCBM. The sparsely covered $MAPbI_3$ nano dots on the ITO/PEDOT:PSS substrate could be readily prepared through spin-casting with low concentration solution of the $MAPbI_3$ perovskite precursor. The outstanding performances were achieved from the TBHJ hybrid device configuration of DIO treated $MAPbI_3$ perovskite nano dots and PCPDTBT －PCBM BHJ composite processed with DIO additive, which played a key role in the development of perovskite structures of $MAPbI_3$ nano dots and induced the (110) directional crystallinity growth of the longitudinal constructive morphologies like nano rods. PCE enhancement of ～28% was achieved as a result of the better $J_{sc}$ and *F.F* when compared to those of conventional BHJ device without $MAPbI_3$ perovskite nano dots. These improved photovoltaic performances originated from the higher quantum efficiencies contributed by the charge transfer from nanostructured $MAPbI_3$ perovskite to PCBM. These TBHJs composed of nanostructured $MAPbI_3$ perovskite, PCPDTBT, and PCBM could also facilitate the exciton dissociation in the multi-BHJ system between $MAPbI_3$ perovskite, PCPDTBT, and PCBM. We believe that the results of this study introduce a new direction for the development of high efficiency OSCs. Further studies on the interfacial photophysics, distribution, and orientation between materials in TBHJ hybrid solar cells are underway.

## E. Reference

[1] Krebs, F. C. *Sol. Energy Mater. Sol. Cells* **2009**, *93*, 394－3412.

[2] Arias, A. C.; Mackenzie, J. D.; McCulloch, I.; Rivnay, J.; Salleo, *Chem. Rev.* **2010**, *110*, 3－324.

[3] He, Z.; Zhong, C.; Su, S.; Xu, M.; Wu, H.; Cao, Y. *Nat. Photonics* **2012**, *6*, 593－5597.

[4] Price, S. C.; Stuart, A. C.; Yang, L.; Zhou, H.; You, W. *J. Am. Chem. Soc.* **2011**, *133*, 4625－44631.

[5] Ma, W.; Yang, C.; Gong, X.; Lee, K.; Heeger, A. J. *Adv. Funct. Mater.* **2005**, *15*, 1617－11622.

[6] Yang, C.; Lee, J. K.; Heeger, A. J.; Wudl, F. *J. Mater. Chem.* **2009**, *19*, 5416－55423.

[7] Lee, K.; Kim, J. Y.; Park, S. H.; Kim, S. H.; Cho, S.; Heeger, A. J. *Adv. Mater.* **2007**, *19*, 2445－2449.

[8] Lee, J. K.; Ma, W. L.; Brabec, C. J.; Yuen, J.; Moon, J. S.; Kim, J. Y.; Lee, K.; Bazan, G. C.; Heeger, A. J. *J. Am. Chem. Soc.* **2008**, *130*, 3619－33623.

[9] Jung, H. S.; Park, N. G. *Small* **2015**, *11*, 10－125.

[10] Burschka, J.; Pellet, N.; Moon, S. J.; Humphry-Baker, R.; Gao, P.; Nazeeruddin, M. K.; Grätzel, M. *Nature* **2013**, *499*, 316－3319.

[11] Jeon, N. J.; Noh, J. H.; Kim, Y. C.; Yang, W. S.; Ryu, S.; Seok, S. I. *Nat. Mater.* **2014**, *13*, 897－8903.

[12] Liu, M.; Johnston, M. B.; Snaith, H. J. *Nature.* **2013**, *501*, 395－3397.

[13] Ahn, N.; Son, D. Y.; Jang, I. H.; Kang, S. M.; Choi, M.; Park, N. G. *J. Am. Chem. Soc.* **2015**, *137*, 8696－88699.

[14] Laban, W. A.; Etgar, L. *Energy Environ. Sci.* **2013**, *6*, 3249－43253.

[15] Shi, J.; Dong, J.; Lv, S.; Xu, Y.; Zhu, L.; Xiao, J.; Xu, X.; Wu, H.; Li, D.; Luo, Y.; Meng, Q. *Appl. Phys. Lett.* **2014**, *104*, 063901.

[16] Mei, A.; Li, X.; Liu, L.; Ku, Z.; Liu, T.; Rong, Y.; Xu, M.; Hu, M. Chen,

J.; Yang, Y. et al. *Science* **2014**, *18*, 295－5298.

[17] Jeng, J. Y.; Chiang, Y. F.; Lee, M. H.; Peng, S. R.; Guo, T. F.; Chen, P.; Wen, T. C. *Adv. Mater.* **2013**, *25*, 3727－33732.

[18] Stranks, S. D.; Eperon, G. E.; Grancini, G.; Menelaou, C.; Alcocer, M. J. P.; Leijtens, T.; Herz, L. M.; Petrozza, A.; Snaith, H. J. *Science* **2013**, *342*, 341－3344.

[19] Xing, G.; Mathews, N.; Sun, S.; Lim, S. S.; Lam, W. M.; Grä4tzel, M.; Mhaisalkar, S.; Sum, T. C. *Science* **2013**, *342*, 344－3347.

[20] Kojima, A.; Teshima, K.; Shirai, Y.; Miyasaka, T. *J. Am. Chem. Soc.* **2009**, *131*, 6050－66051.

[21] Pang, S.; Hu, H.; Zhang, J.; Lv, S.; Yu, Y.; Wei, F.; Qin, T.; Xu, H.; Liu, Z.; Cui, G. *Chem. Mater.* **2014**, *26*, 1485－11491.

[22] Qin, P.; Paek, S.; Dar, M. I.; Pellet, N.; Ko, J.; Gräktzel, M.; Nazeeruddin, M. K. *J. Am. Chem. Soc.* **2014**, *136*, 8516－88519.

[23] Sun, S.; Salim, T.; Mathews, N.; Duchamp, M.; Boothroyd, C.; Xing, G.; Sum, T. C.; Lam, Y. M. *Energy Environ. Sci.* **2014**, *7*, 399－3407.

[24] Seo, J.; Park, S.; Kim, Y. C.; Jeon, N. J.; Noh, J. H.; Yoon, S. C.; Seok, S. I. *Energy Environ. Sci.* **2014**, *7*, 2642－42646.

[25] Paek, S.; Cho, N.; Choi, H.; Jeong, H.; Lim, J. S.; Hwang, J. Y.; Lee, J. K.; Ko, J. *J. Phys. Chem. C.* **2014**, *118*, 25899－225905.

[26] Liu, Y.; Hong, Z.; Chen, Q.; Chang, W.; Zhou, H.; Song, T. B.; Young, E.; Yang, Y. M.; You, J.; Li, G.; Yang, Y. *Nano Lett.* **2015**, *15*, 662－6668.

[27] Liu, C.; Wang, K.; Du, P.; Yi, C.; Meng, T.; Gong, X. *Adv. Energy Mater.* **2015**, *5*, 1402024.

[28] Liang, P.; Liao, C.; Chueh, C.; Zuo, F.; Williams, S. T.; Xin, X.; Lin, J.; Jen, A. K.-Y. *Adv. Mater.* **2014**, *26*, 3748－33754.

[29] He, Z.; Zhong, C.; Su, S.; Xu, M.; Wu, H. Cao, Y. *Nat. Photonics* **2012**, *6*, 593－5597.

# Chapter 2.

# Improved Efficiency of Solution-Processed Bulk-Heterojunction Organic Solar Cells and Planar-Heterojunction Perovskite Solar Cells with Efficient Hole-Extracting Si Nanocrystals

# A. Introduction

Solution-processed solar cells have attracted great interest because of their easy and inexpensive manufacturing processes, including versatile methods such as inkjet, doctor-blade, and roll-to-roll printing.[1-2] Recently, considerable efforts have been focused on achieving competitive power conversion efficiencies (PCEs) competitive with those of conventional silicon-based solar cells. As a promising alternative, solution-processed organic solar cells (OSCs) have exhibited excellent PCEs of ~10% for the low-bandgap poly(thieno[3,4-*b*]thiophene-*alt*-benzo -dithiophene) (PTB7-Th) based semiconducting polymer and [6,6]-phenyl -$C_{(61or71)}$-butyric acid methyl ester ($PC_{(61or71)}BM$) bulk-heterojunctions (BHJs).[3] Very recently, solution-processable organometal halide perovskite solar cells (PrSCs), especially those containing $(CH_3NH_3)PbX_3$ [$MAPbX_3$, (X = Cl, Br, I)] have also received considerable attention because they have exhibited exceptional PCEs of over 15%.[4-6] Specifically, p-i-n type PrSCs are often fabricated using planar heterojunction (PHJ) bilayer structures of perovskite materials and PCBM. [7] Because these BHJ OSCs and PHJ PrSCs have quite similar device configuration comprising of indium tin oxide (ITO)/poly(3,4-ethylenedioxy -thiophene):poly(styrenesulfonate)(PEDOT:PSS)/donor:acceptor/Al,[8] various strategies have been adopted to obtain high PCEs. Examples include the development of high-performance semiconducting polymer materials or perovskite materials,[9-12] effective functions with surface plasmon resonances,[13-14] charge transport,[15-16] and charge extraction[17-18] in device structures, and morphological engineering by thermal annealing,[19-20] solvent-casting,[5,21] or processing additives.[22-23]

Among these approaches, efficient charge-extraction materials, which can effectively suppress carrier recombination or trapping, have been often employed to achieve enhanced PCEs.[24] This is because the extraction efficiency for charge carriers separated from excitons in interfaces of donor and acceptor has

been known to be one of the influential factors affecting the PCEs of these solution-processed solar cells. In particular, wide-bandgap inorganic nanocrystals (NCs) such as $TiO_2$ (or ZnO) and $MoO_3$ have exhibited excellent electron-extracting and hole-extracting features, respectively, in BHJ OSCs and PHJ PrSCs.[25-27] Additionally, inorganic semiconductor NCs such as CdS, CdSe, and PbS, could also be utilized in hybrid solar cells (HSCs) with organic semiconductors because their optical and electronic properties can be tailored through size-dependent bandgap engineering.[28-29] However, owing to the toxicity of these materials, HSCs fabricated with polymer donors using environmentally benign SiNCs as the electron acceptor have been recently reported but they also suffer from lower PCEs than those of BHJ OSCs with PCBM.[30-31] Nonetheless, their highly desirable optical and electronic properties depend on their nanometer-scale size and the carrier concentration induced by doping,[32] which may make their integration into HSCs challenge.

On the other hand, very recently, we reported an efficiency improvement in OSCs with a ternary BHJ (TBHJ) configuration consisting of the nanostructured perovskite-low bandgap polymer-PCBM.[33] A TBHJ device, which was constructed with a semiconducting polymer-PCBM BHJ integrated on perovskite nanostructures exhibited better photovoltaic performance than a BHJ device without perovskite materials because perovskite materials play a key role as electron and hole conductors and photosensitizers.[4-7] Based on these results, we attempted for the first time to utilize Si NCs as hole extraction materials (HEMs) in solution processed BHJ OSCs using a TBHJ device architecture because there is little research on the incorporation of Si NCs in HSCs as HEMs. Additionally, we speculated that this approach can be employed in PHJ PrSCs fabricated using bilayer structures of perovskite materials and PCBM on ITO/PEDOT:PSS substrates.

Herein, we report the efficiency enhancement of solution-processed BHJ OSCs and PHJ PrSCs using hole-extracting Si NCs. Additionally, we compared the

HEM efficacy of undoped Si NCs and p-type Si NCs in these devices. The examined solution-processed BHJ OSCs and PHJ PrSCs had device configurations of ITO/PEDOT:PSS/PTB7-Th:$PC_{71}BM$/Al and ITO/PEDOT:PSS/$MAPbI_3$/$PC_{61}BM$ /Al, respectively, and the Si NC HEMs were spin-cast on an ITO/PEDOT:PSS substrate. Figure 2.1 shows the device architectures of the solution-processed BHJ OSCs and PHJ PrSCs, which were fabricated with Si NC HEMs cast on an ITO/PEDOT:PSS substrate. The sparse coverage of the Si NCs on the ITO/PEDOT:PSS substrate was readily demonstrated by varying the concentration of Si NCs dispersed in a chlorobenzene (CB) solvent. Notably, outstanding performances were observed in the hybrid devices constructed with BHJ (or PHJ) layers on PEDOT:PSS/Si NCs and the Si NCs obviously played a key role for the easy extraction of hole carriers separated from excitons in interfaces of the donors and the PCBM. Specifically, the PCEs of the BHJ OSCs and PHJ PrSCs were enhanced by ~11% and ~23%, respectively, compared with those of the corresponding devices without Si NC HEMs. Furthermore, the highest occupied molecular orbital (HOMO) energy level of p-Si NCs is ~0.16eV higher than that of undoped Si NCs. Therefore, the p-Si NCs showed better balances between the HOMO energy levels of PTB7-Th and $MAPbI_3$ perovskite materials, resulting in optimal PCEs in both BHJ OSCs and PHJ PrSCs.

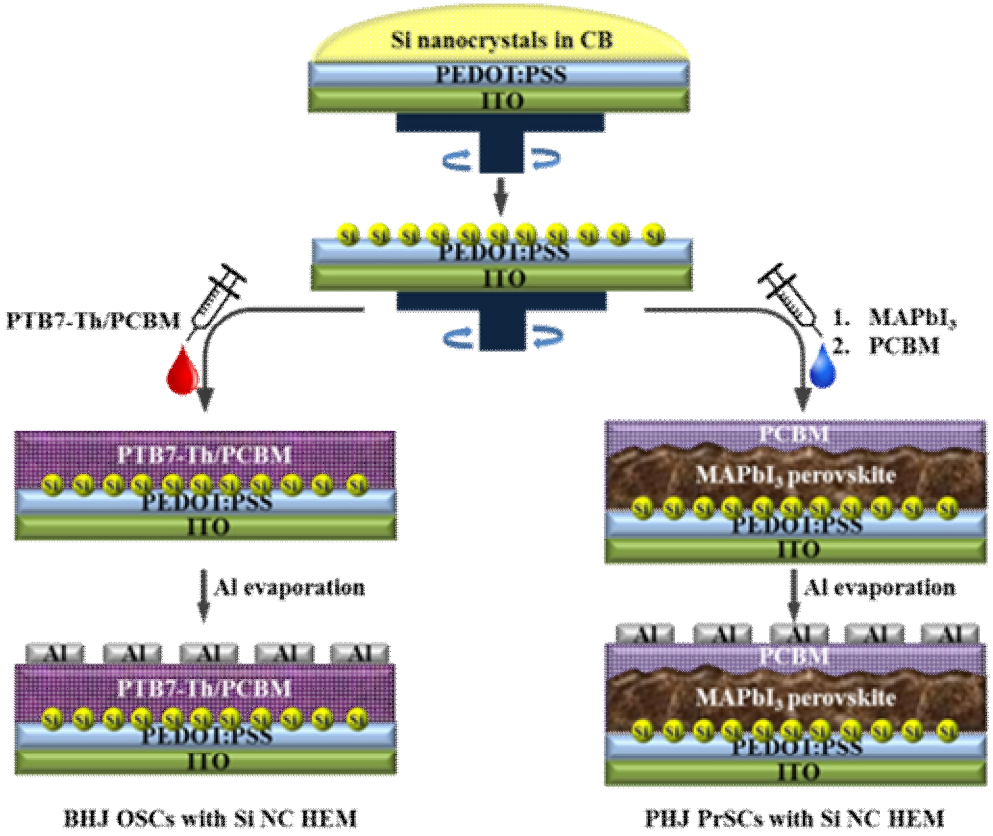


***Figure 2.1*** Schematic descriptions for fabrication of solution-processed BHJ OSCs and PHJ PrSCs device structures with Si NC HEMs.

## B. Experimental methods

### 1. Materials

The $PbI_2$ was purchased from Aldrich and $CH_3NH_3I$ was prepared according to the method reported previously.[8] All solvents were purchased from Sigma-Aldrich, TCI, and Alfa Aesar and were purified using appropriate methods. The $MAPbI_3$ precursor solution was prepared under a nitrogen atmosphere. The PTB7-Th and PCBM were obtained from 1-Material and Nano-C, respectively. B-doped and undoped polycrystalline silicon wafers were purchased from University Wafer.

### 2. Preparation of Si NCs

The Si NCs were produced using a modified electrochemical etching process,[34] using a wafer feedstock that was pulverized while being slowly dipped into a solution of HF and $H_2O_2$. The B-doped and undoped polycrystalline silicon wafers were used to provide p-Si NCs and undoped Si NCs, respectively. These wafers were placed in a bath of n-hexadecane and ultrasonicated to form a suspension of small Si particles, which were transferred from the n-hexadecane to CB before use.

### 3. Measurements and instruments

Transmittance spectra were recorded using a Perkin-Elmer Lambda 2S ultraviolet-visible spectrometer. The surface morphologies were imaged using a field emission scanning electron microscope (FESEM, Nova nanoSEM 450, FEI, Netherlands) and a high-resolution transmission electron microscope (HRTEM, G2 F20, FEI Tecnai, Netherlands). The HOMO of the materials was estimated from their ionization potential, which was measured using ultraviolet photoelectron spectroscopy (UPS) in air (surface analyzer, AC2, Riken Keiki, Co., Ltd., Japan).

The solar cell efficiencies were determined under simulated 100 $mW \cdot cm^{-2}$ AM 1.5G irradiation from a Xe arclamp with an AM 1.5 global filter. The simulator irradiance was characterized using a calibrated spectrometer and the illumination intensity was set using a silicon diode with an integrated KG1 optical filter certified by the National Renewable Energy Laboratory. The spectral mis match factors were calculated to belower than 5% for all devices. The short circuit currents were also observed to be with in 5% of the values calculated using the integrated external quantum efficiency (EQE) spectra and the solar spectrum. The applied potential and cell currents were measured using a Keithley 2400 digital source meter. The current density-voltage (*J-V*) curves were measured at a voltage settling time of 100ms. The EQEs were measured by under filling the device are a using a reflective microscope objective to focus the light output from a 75W Xe lamp, a monochromator, and an optical chopper. The photocurrent was measured using a lock-in amplifier. The absolute photon flux was determined using a calibrated silicon photodiode and was recorded for 5 s per point (80 points) between350-1100nm.

## 4. Device fabrication

The ITO-coated glass substrates were cleaned with detergent, ultrasonicated in acetone and isopropyl alcohol, and dried overnight in an oven. An aqueous solution of PEDOT:PSS (Heraeus, Clevios P VP.AI 4083) was spin-cast onto the ITO substrates to form a film ~35 nm in thickness. The substrate was dried in air at 140 °C for 10 min and was transferred into a glove box for spin-casting of the Si NC solution. The Si NC solution was prepared in CB at 0.024, 0.034, 0.057, 0.171, and 0.854 mg/ml and was uniformly dispersed by sonication for 10 min before use. These were spin-cast at 2000 rpm for 60 s and dried at 60 °C for 10 min. A BHJ active layer and a PHJ bilayer were deposited on the ITO/PEDOT:PSS/Si NC substrate for OSCs and PrSCs, respectively, as follows: for the OSC, a PTB7-Th:$PC_{71}BM$ BHJ blend solution (weight ratio, 1:1.5) with

diiodooctane additive (2 vol%) was spin-cast at 2000 rpm and was subsequently heat-treated at 80 °C for 10 min. For the PrSCs, a $MAPbI_3$ precursor solution was prepared using $PbI_2$ and $CH_3NH_3I$ (molar ratio 1:1) in dimethylformamide at 60 wt% and stirred at 60 °C for 12h. The $MAPbI_3$ perovskite films were produced by spin-casting at 5000 rpm for 30 s using the $MAPbI_3$ precursor solution and by dripping of CB; they were then dried on a hot-plate at 100 °C for 10 min. The $PC_{61}BM$ solution was spin-cast on top of the $MAPbI_3$ layer and the process was followed by heat-treatment at 80 °C for 10min. Finally, an Al metal electrode of thickness ~100 nm was deposited on top of the PTB7-Th:$PC_{71}BM$ BHJ film and $MAPbI_3$/$PC_{61}BM$ PHJ film at low pressure (below $10^{-6}$ Torr).

## C. Result and discussion

Figure 2.2 shows (a) HRTEM images (inset) of the synthesized Si NCs and the ultraviolet photoelectron spectra of the p-Si NCs and undoped Si NCs and (b) the HOMO energy levels of these Si NCs. The HOMO values were estimated from the ionization potentials, which were obtained using UPS analysis, and compared with those of PTB7-Th and $MAPbI_3$ materials (see Figure 2.3). The Si NCs were prepared by a modified electro chemical etching method,[34] using a wafer feedstock that was pulverized while being slowly dipped into a solution of HF and $H_2O_2$. The particles were produced by Si:H passivation. Additionally, these Si nanoparticles had polycrystalline morphologies because they were fabricated using polycrystalline silicon wafer resources. As shown in Figure 2.2.a (inset), the small particulate Si NCs had an average size of ~5nm, which was determined by dynamic light scattering analysis as shown in Figure 2.4, and appeared to be agglomerated to 50~100 nm because of their high surface energy.

In this work, we used two types (p-type and undoped) Si NCs to evaluate their efficacy as HEM materials for solution-processed BHJ OSCs and PHJ PrSCs. Although Si NCs are often prepared with various bottom-up synthesis techniques, fabricating Si NCs whilst retaining Si:H surface passivation is very difficult. However, the electrochemical etching process used in this work readily provided p-Si NCs and undoped Si NCs from commercially available B-doped and undoped polycrystalline silicon wafers, respectively. The light emissions of these Si NCs were examined using their photoluminescence spectra (Figure 2.5). Because these particles were not smaller than the typical Bohr radius of the exciton of silicon, they did not exhibit a discrete density of states; hence, no size-dependent quantum confinement effects were expected to occur.[35] However, the luminescence in here is designed to result from the surface states of the particles. As shown in Figure 2.2.b, the HOMO of p-Si NCs is -4.79 eV, which is ~0.16 eV higher than the value (-4.95 eV) of undoped Si NC. The HOMOs

of PTB7-Th and $MAPbI_3$ materials were obtained as -4.99 eV and -5.22 eV, respectively, under the same measuring conditions.[36] These results indicate that the HOMO value of p-Si NCs could have a better balance with those of PTB7-Th and $MAPbI_3$ perovskite materials than undoped Si NCs, indicating a better performance of BHJ OSCs and PHJ PrSCs as HEMs.

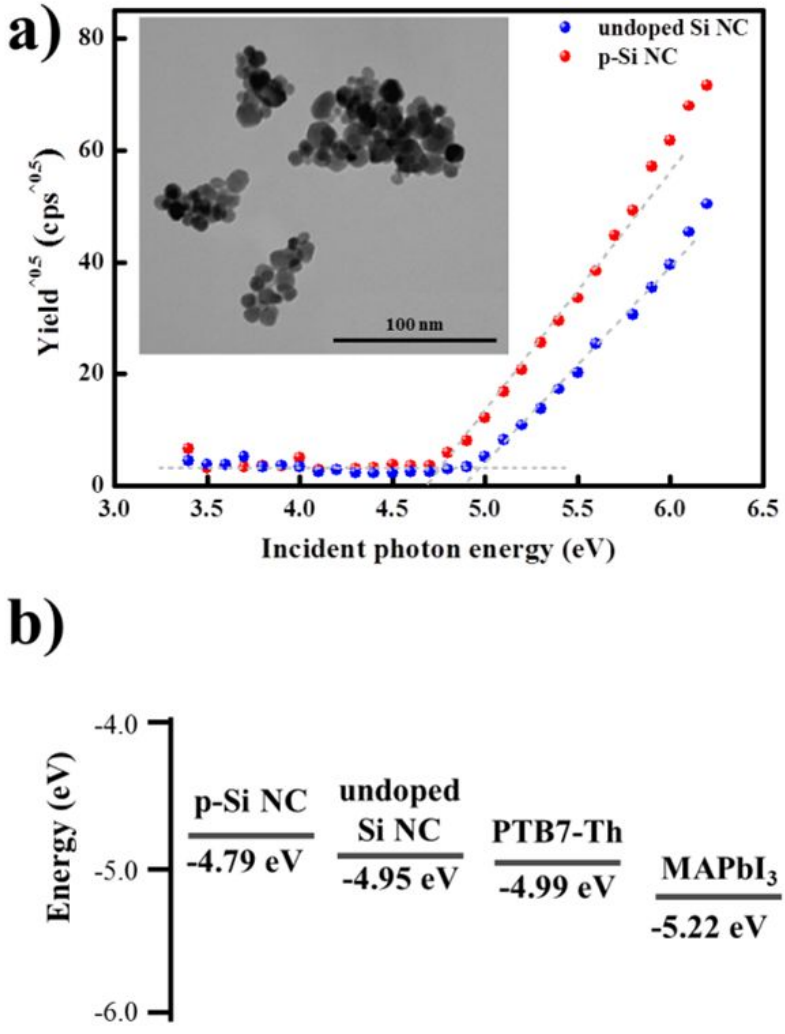


***Figure 2.2*** (a) HRTEM images (inset) of synthesized Si NCs (~5nm) and ultraviolet photoelectron spectra of p-type Si NCs and undoped Si NCs and (b) HOMO energy levels of these Si NCs, PTB7-Th, and $MAPbI_3$ materials.

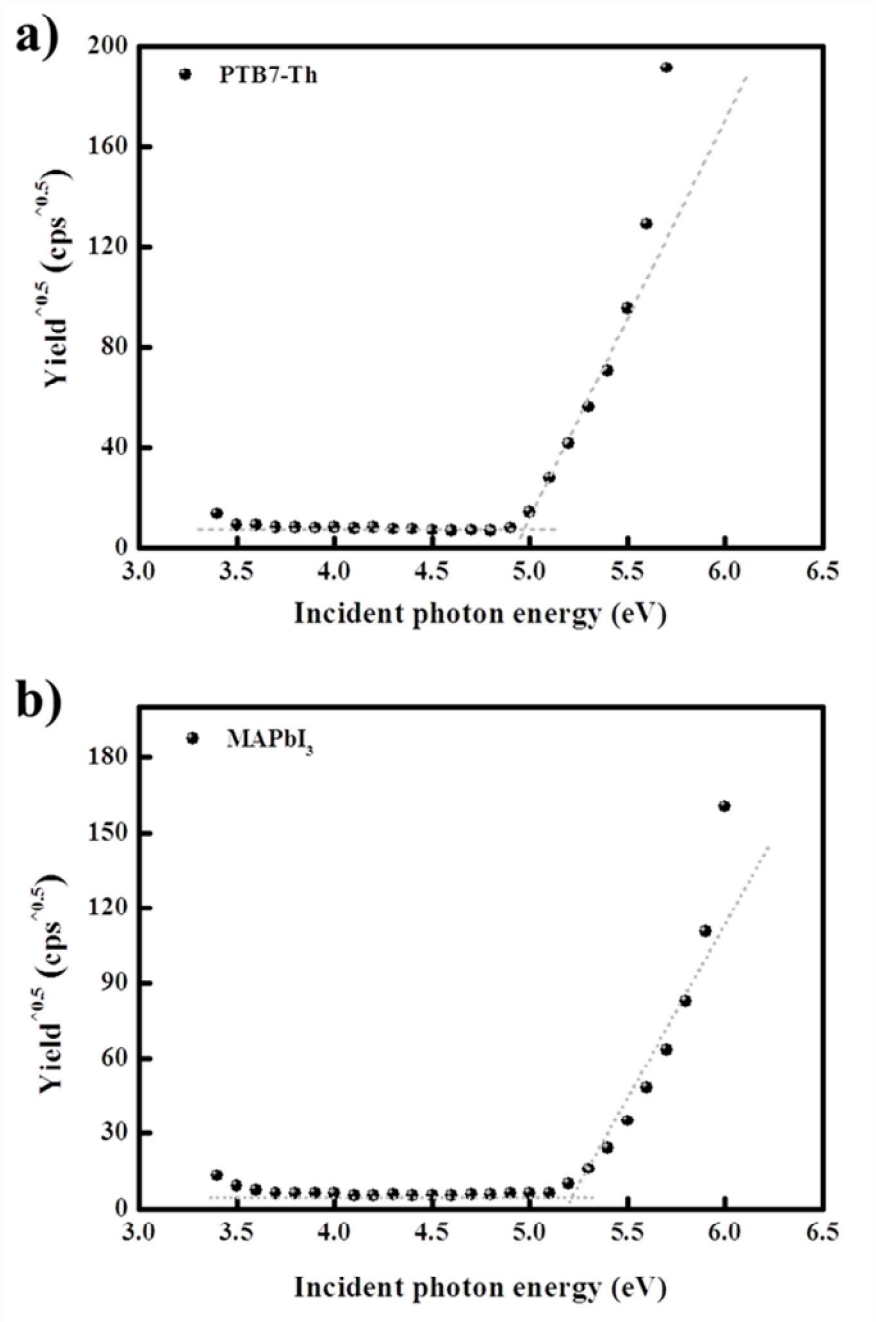


***Figure 2.3*** The UPS spectra of (a) PTB7-Th and (b) $MAPbI_3$ materials, which were estimated from the ionization potentials.

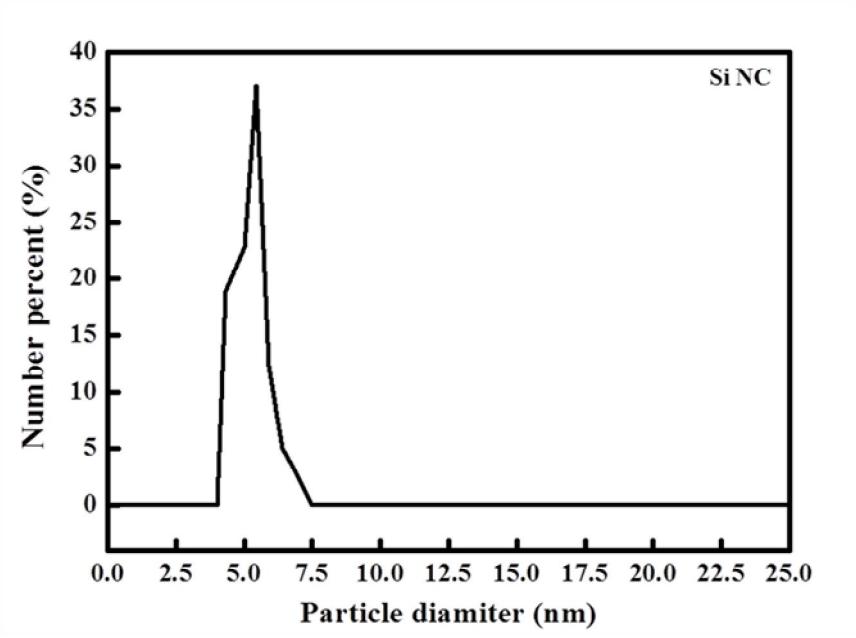


***Figure 2.4*** DLS spectra of Si NCs prepared using a modified electrochemical etching method.

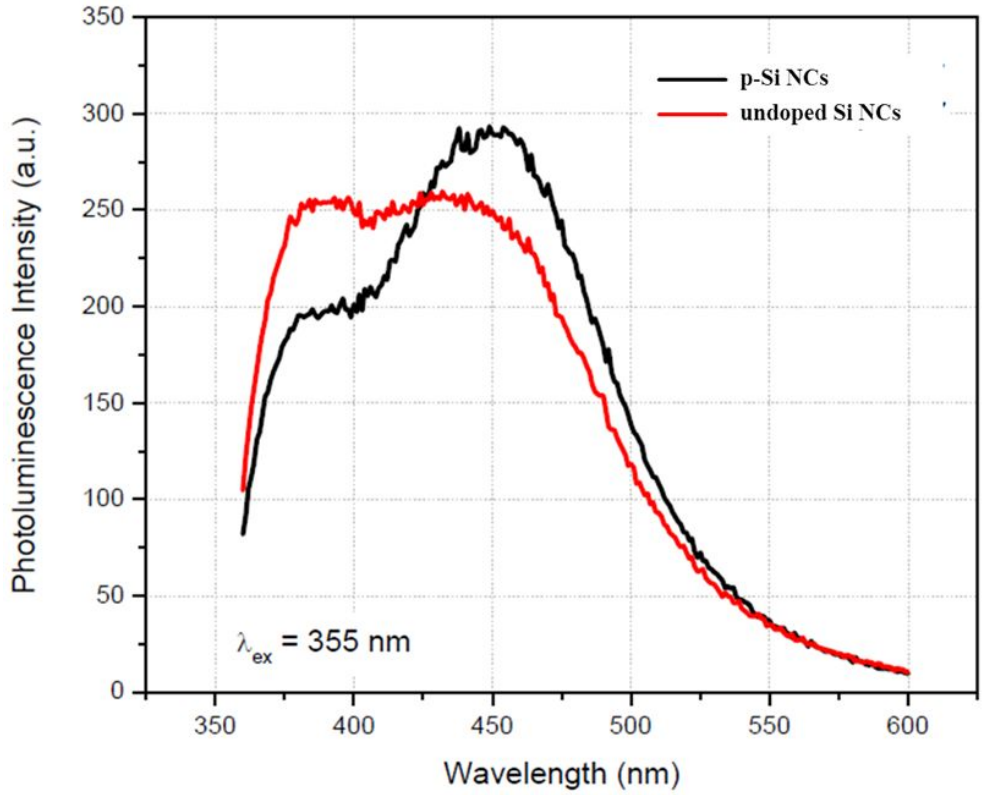


***Figure 2.5*** Photoluminescence spectra of p-Si NCs and undoped Si NCs, which were obtained from B-doped and undoped polycrystalline silicon wafers, respectively, by a modified electrochemical etching approach.

Figure 2.6 presents FESEM surface images of Si NCs spin-cast on the ITO/PEDOT:PSS substrates for various Si NCs concentrations (0.024, 0.034, 0.057, 0.171, and 0.854 mg/ml) in CB. As shown in Figure 2.6, the Si NCs cast on the ITO/PEDOT:PSS substrates exhibited a sparser surface coverage at low concentrations and a dense surface coverage for concentration above 0.8 mg/ml; however, they exhibited non-uniform film morphologies for Si NC agglomerates of 50~100 nm as shown in Figure 2.2.a (inset). Based on these results, we employed the discussed PEDOT:PSS/Si NCs HEM layer in both the OSCs and the PrSCs fabricated from the PTB7-Th:$PC_{71}BM$ BHJ film and $MAPbI_3/PC_{61}BM$ PHJ film, respectively.

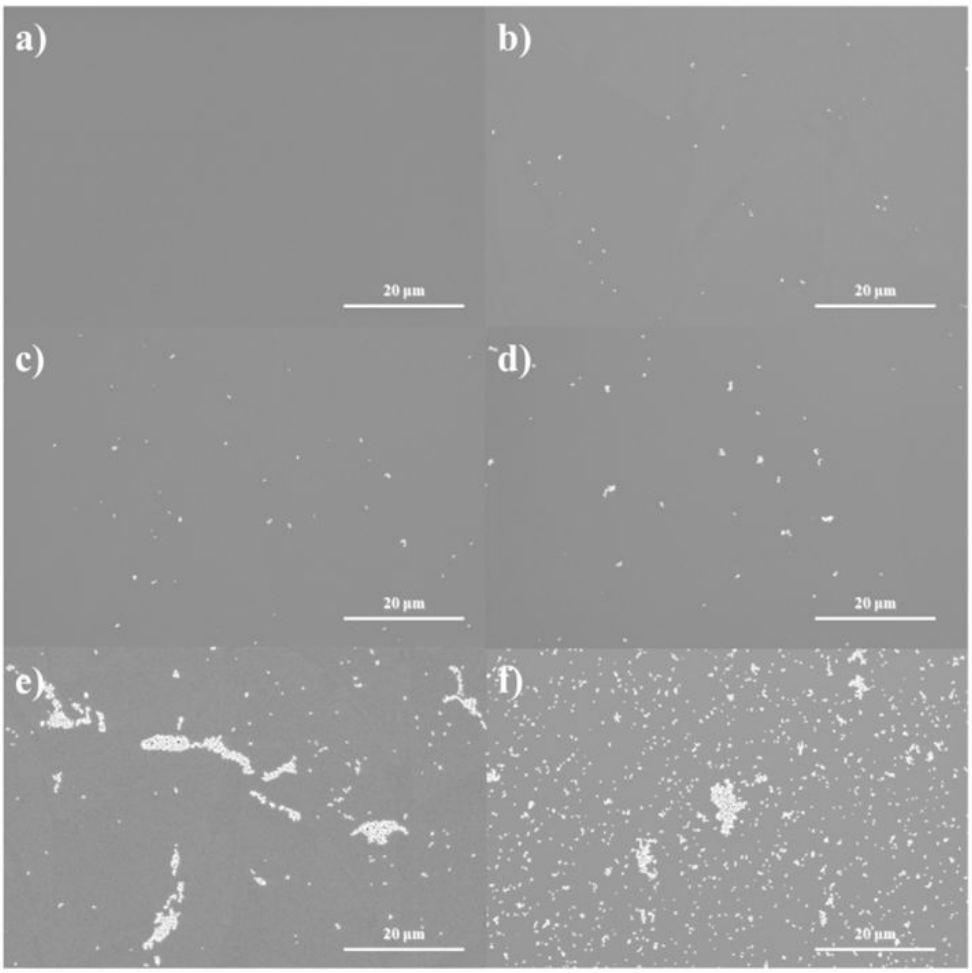


***Figure 2.6*** FESEM surface images of Si NCs spin-cast on the ITO/PEDOT:PSS substrates for various Si NCs concentrations ((a) 0, (b) 0.024, (c) 0.034, (d) 0.057, (e) 0.171, and (f) 0.854 mg/ml) in CB.

Figure 2.7 shows the photovoltaic performances of these BHJ OSC and PHJ PrSC devices with PEDOT:PSS/Si NC HEM layers fabricated at various concentrations (0.024, 0.034, 0.057, 0.171, and 0.854 mg/ml %) of p-Si NCs in CB solvent; these are compared with the performances of the corresponding devices without Si NCs. The displayed values were determined from the average of individual hybrid solar cells fabricated under conditions optimized for the construction of BHJ OSCs and PHJ PrSCs without Si NCs materials (see Table 2.1)

The surface coverage on the substrate can significantly affect the photovoltaic performance of the BHJ OSCs and PHJ PrSCs as shown in Figure 2.7. Additionally, both the BHJ OSCs and the PHJ PrSCs with PEDOT:PSS/p-Si NC HEM layers that were fabricated using a p-Si NC solution of 0.034 mg/ml exhibited the most improved photovoltaic performance compared to the devices without Si NCs. The results indicate that the increased PCE of the BHJ OSCs and PHJ PrSCs with PEDOT:PSS/p-Si NC HEM layers was obviously induced by their significantly enhanced photocurrents. However, the BHJ OSC and PHJ PrSC devices fabricated with solution concentrations higher than 0.170 mg/ml exhibited some degraded photovoltaic performances owing to short-circuit current density ($J_{sc}$) losses and both the open-circuit voltage ($V_{oc}$) and fill factor ($F.F$), respectively.

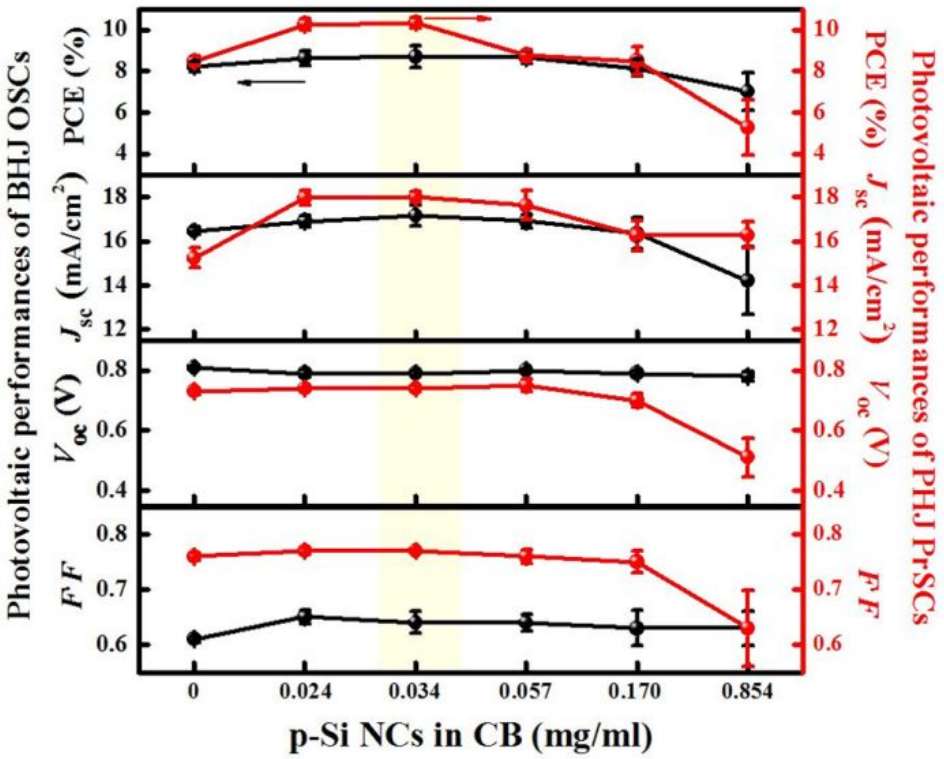


***Figure 2.7*** Photovoltaic performances of these BHJ OSC (black) and PHJ PrSC (red) devices with PEDOT:PSS/p-Si NC HEM layers fabricated at various concentrations (0, 0.024, 0.034, 0.057, 0.171, and 0.854 mg/ml) of Si NCs in CB solvent.

***Table 2.1*** Photovoltaic performances of these BHJ OSC (black) and PHJ PrSC (red) devices with PEDOT:PSS/p-Si NC HEM layers fabricated at various concentrations (0, 0.024, 0.034, 0.057, 0.171, and 0.854 mg/ml) of Si NCs in CB solvent.[a]

| Devices | p-Si NC (mg/mL) | $J_{sc\ ave/max}$ (mA/cm$^2$) | $V_{oc\ ave/max}$ (V) | $F{\cdot}F_{ave/max}$ | $\eta_{ave/max}$ (%) |
|---|---|---|---|---|---|
| PTB7-Th :$PC_{71}BM$ BHJ OSC | 0 | 16.46/16.62 | 0.81/0.82 | 0.61/0.62 | 8.21/8.35 |
| | 0.024 | 16.89/17.16 | 0.79/0.80 | 0.65/0.66 | 8.21/8.95 |
| | 0.034 | 17.16/17.78 | 0.79/0.80 | 0.64/0.66 | 8.70/9.25 |
| | 0.057 | 16.90/17.21 | 0.80/0.80 | 0.64/0.66 | 8.65/8.96 |
| | 0.171 | 16.34/17.04 | 0.79/0.80 | 0.63/0.66 | 8.14/8.54 |
| | 0.854 | 14.20/15.72 | 0.78/0.80 | 0.63/0.66 | 7.00/7.92 |
| $MAPbI_3$ /$PC_{61}BM$ PHJ PrSC | 0 | 15.23/15.69 | 0.73/0.74 | 0.76/0.77 | 8.47/8.59 |
| | 0.024 | 17.96/18.29 | 0.74/0.74 | 0.77/0.78 | 10.25/10.53 |
| | 0.034 | 18.00/18.22 | 0.74/0.75 | 0.77/0.78 | 10.33/10.52 |
| | 0.057 | 17.62/18.29 | 0.75/0.77 | 0.76/0.77 | 8.76/9.04 |
| | 0.171 | 16.24/16.92 | 0.70/0.72 | 0.75/0.77 | 8.49/9.16 |
| | 0.854 | 16.27/16.86 | 0.51/0.57 | 0.63/0.70 | 5.27/6.61 |

[a]The performances are determined under simulated 100 mW·cm$^{-2}$ AM 1.5 illumination. The light intensity using calibrated standard silicon solar cells with aproactive window made from KG5 filter glass traced to the NREL. The active area of device is 4.5mm$^2$.

Next, we prepared two types (p-type and undoped) Si NCs and utilized them in solution-processed BHJ OSCs and PHJ PrSCs fabricated from the PTB7-Th:$PC_{71}BM$ BHJ film and $MAPbI_3/PC_{61}BM$ PHJ films to evaluate the Si NC HEM efficacy. Figure 2.8 presents the *J-V* curves of BHJ OSCs and PHJ PrSCs fabricated under optimized processing conditions with (p-type and undoped) Si NCs (0.034 mg/ml) deposited on PEDOT:PSS substrates; the curves were measured under AM 1.5 irradiation (100 $mW \cdot cm^{-2}$) and are compared those (black) of devices without Si NCs. The corresponding values are summarized in Table 2.2. As shown in Figure 2.8 and Table 2.2, the BHJ OSC devices fabricated with undoped Si NCs showed a ~6 % PCE enhancement compared with the BHJ OSCs without Si NC HEMs, with a PCE (best/average) of 8.85/8.31 % with $J_{sc}$ = 17.3/16.9 $mA \cdot cm^{-2}$, $V_{oc}$ = 0.80/0.79 V, and *F.F* = 0.64/0.63. The devices with p-Si NCs exhibited PCEs enhanced by ~11 %, with PCE = 9.25/8.70 % with $J_{sc}$ = 17.8/17.2 $mA \cdot cm^{-2}$, $V_{oc}$ = 0.80/0.79 V, and *F.F* = 0.66/0.64. The corresponding values of the BHJ OSCs without Si NC HEMs were PCE = 8.35/8.21 % with $J_{sc}$ = 16.6/16.5 $mA \cdot cm^{-2}$, $V_{oc}$ = 0.82/0.81 V, and *F.F* = 0.62/0.61. Moreover, the PHJ PrSC devices fabricated with undoped Si NCs and p-Si NCs exhibited enhanced PCEs by ~22 % and ~23 %; for the former, we measured a PCE (best/average) of 10.52/10.33 % with $J_{sc}$ = 18.2/18.0 $mA \cdot cm^{-2}$, $V_{oc}$ = 0.75/0.74 V, and *F.F* = 0.78/0.77; for the latter, PCE = 10.49/10.17 % with $J_{sc}$ = 17.7/17.3 $mA \cdot cm^{-2}$, $V_{oc}$ = 0.74/0.73 V, and *F.F* = 0.80/0.79. The corresponding values determined for the PHJ PrSCs without Si NC HEMs were PCE = 8.59/8.47 % with $J_{sc}$ = 15.7/15.2 $mA \cdot cm^{-2}$, $V_{oc}$ = 0.74/0.73 V, and *F.F* = 0.77/0.76. From these results, the OSC devices fabricated with PTB7-Th:$PC_{71}BM$ BHJ film cast on PEDOT:PSS/p-Si NCs obviously presented better photovoltaic performances than those with PEDOT:PSS/undoped Si NCs, where as the PrSC devices fabricated with $MAPbI_3/PC_{61}BM$ PHJ film showed similar HEM efficacy for both p-Si NCs an undoped Si NCs. This indicates a significant enhancement of the photovoltaic performances of the PHJ PrSC

devices compared with those of BHJ OSCs with Si NC HEMs. This behavior might originate from the balances of the HOMO values of the p-Si NCs and undoped Si NCs with those of PTB7-Th and $MAPbI_3$ perovskite materials as shown in Figure 2.2b.

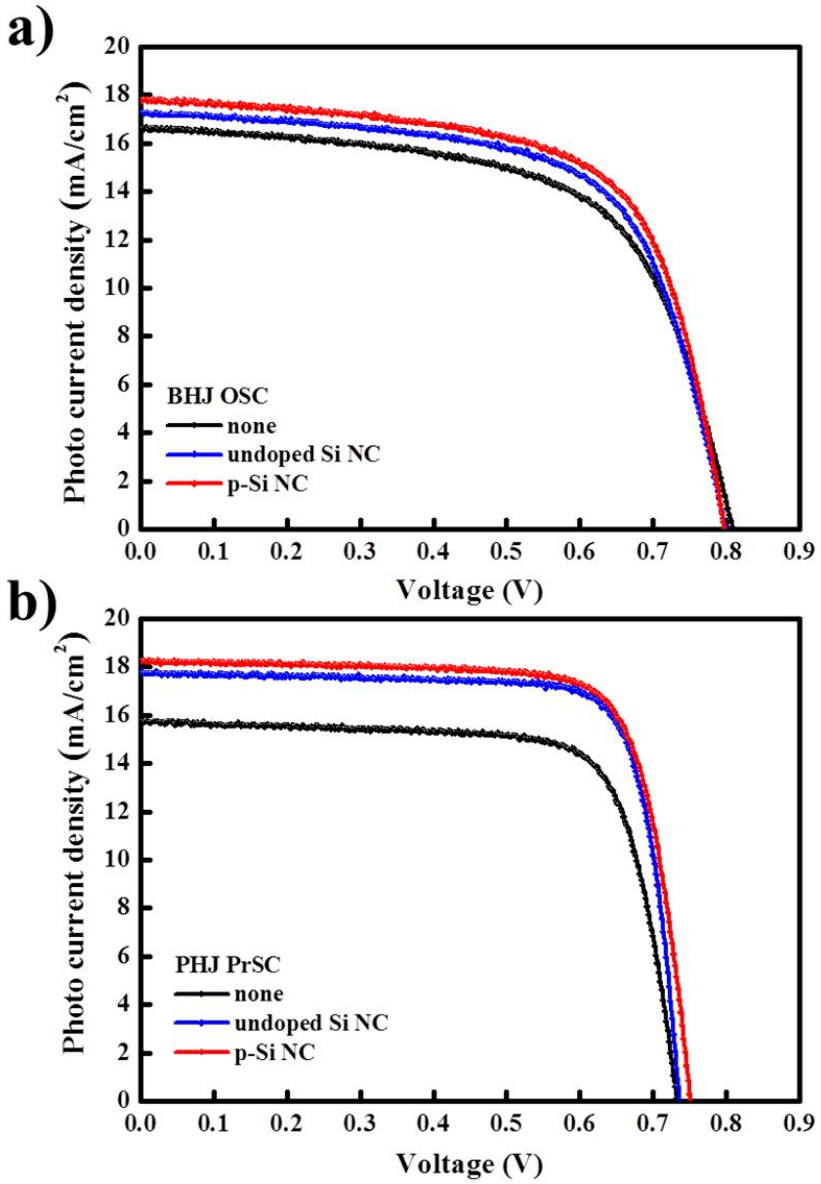


***Figure 2.8*** (a) Distribution *J-V* curves under AM 1.5 irradiation (100 mWcm$^{-2}$) for (a) BHJ OSCs and (b) PHJ PrSCs fabricated under optimized processing conditions with (p-type (red) and undoped (blue)) Si NCs (0.034mg/ml) deposited on PEDOT:PSS substrate and compared those (black) without Si NCs.

***Table 2.2*** Photovoltaic performances of BHJ OSCs and PHJ PrSCs fabricated with/without Si NCs HEMs cast on ITO/PEDOT:PSS.[a]

| Device | Si NCs | $J_{sc\ best/ave}$ ($mAcm^{-2}$) | $V_{oc\ best/ave}$ (V) | $F.F_{\ best/ave}$ | $\eta_{\ best/ave}$ (%) |
|---|---|---|---|---|---|
| BHJ OSC | none | 16.6/16.5 | 0.82/0.81 | 0.62/0.61 | 8.35/8.21 |
| | undoped | 17.3/16.9 | 0.80/0.79 | 0.64/0.63 | 8.85/8.31 |
| | p-type | 17.8/1.72 | 0.80/0.79 | 0.66/0.64 | 9.25/8.70 |
| PHJ PrSC | none | 15.7/15.2 | 0.74/0.73 | 0.77/0.76 | 8.59/8.47 |
| | undoped | 17.7/17.3 | 0.74/0.73 | 0.80/0.79 | 10.49/10.17 |
| | p-type | 18.2/18.0 | 0.75/0.74 | 0.78/0.77 | 10.52/10.33 |

[a]The performances are determined under simulated 100 $mW \cdot cm^{-2}$ AM 1.5 illumination. The light intensity using calibrated standard silicon solar cells with aproactive window made from KG5 filter glass traced to the NREL. The active area of device is $4.5mm^2$.

To clarify the function of Si NCs as HEMs, we investigated the hole mobilities of PTB7-Th:$PC_{71}BM$ BHJ in BHJ OSCs with/without Si NC HEMs; these mobilities were extracted from the space-charge limited current (SCLC) *J-V* characteristics, which were obtained in the dark for hole-only devices, ITO/PEDOT:PSS/Si NCs/PTB7-Th:$PC_{71}BM$/Au.

Figure 2.9 shows (a) SCLC *J-V* characteristics obtained in the dark for hole-only devices, ITO/PEDOT:PSS/Si NCs/PTB7-Th:$PC_{71}BM$/Au and (b) EQE spectra of BHJ OSCs fabricated with/without Si NCs under optimized processing conditions. The dark-current characteristics between PEDOT:PSS and PTB7-Th:$PC_{71}BM$ layers of these hole-only devices with/without Si NCs were obtained as a function of the bias corrected for the built-in voltage, which was determined from the difference in workf unction between Au and the PEDOT:PSS-coated ITO. As shown in Figure 2.7.a, their SCLC behavior is characterized by the Mott－Gurneylaw (1).[37]

$$J=(9/8)\varepsilon\cdot\mu(V^2/L^3) \quad (1)$$

where $\varepsilon$ is the static dielectric constant of the medium, and $\mu$ is the carrier mobility. The hole mobilities of the PTB7-Th:$PC_{71}BM$ BHJ films cast on p-Si NCs and undoped Si NCs calculated with the Mott-Gurney law ($\varepsilon = 3\varepsilon_0$) were $4.42\times10^{-4}$, and $4.00 \times 10^{-4}cm^2\cdot V^{-1}\cdot s^{-1}$, respectively. These values are rather higher than that obtained ($3.18\times10^{-4}cm^2\cdot V^{-1}\cdot s^{-1}$) for the films without Si NC HEMs. These results suggest that a well-balanced electron and hole mobility in the PTB7-Th:$PC_{71}BM$ BHJ system can be demonstrated by the Si NC HEMs which could facilitate the hole-extraction from the polymer to the PEDOT:PSS, which could closely correlate with the integrated EQE spectra of these devices shown in Figure 2.9.b.

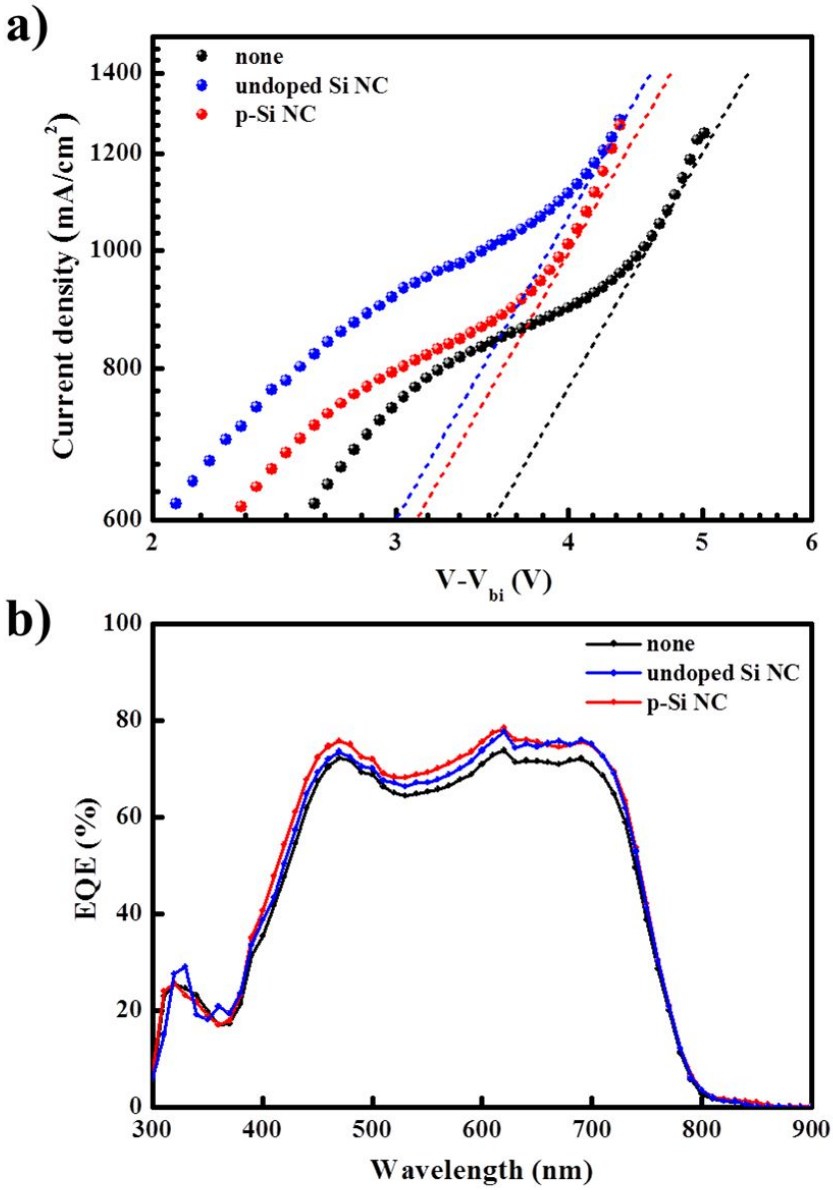


***Figure 2.9*** SCLC *J-V* characteristics obtained in the dark for hole-only devices, ITO/PEDOT:PSS/SiNCs/PTB7-Th:$PC_{71}BM$/Au and (b) EQE spectra of BHJ OSCs fabricated with/without Si NCs under optimized processing conditions.

## D. Conclusion

We demonstrated the efficiency improvement in solution-processed BHJ OSCs and PHJ PrSCs by implementing Si NCs for efficient hole extraction. Additionally, we compared the HEM efficacy of undoped Si NCs and p-Si NCs in these devices. The Si NCs were prepared with an average size of ~5 nm using a modified electrochemical etching method that provided p-Si NCs and undoped Si NCs from easily available B-doped and undoped polycrystalline silicon wafers, respectively, whilst retaining Si:H surface passivation. The p-Si NCs had a HOMO energy level that was ~0.16 higher than that of undoped Si NCs, showing better balances with the HOMO energy levels of the PTB7-Th and $MAPbI_3$ perovskite materials. The surface coverage of the Si-NCs on the substrate significantly affected the photovoltaic performance of the BHJ OSCs and PHJ PrSCs, resulting in PCEs enhanced by ~6 % and ~11 % in the BHJ OSCs with undoped Si NCs and p-Si NCs, respectively, and by ~22 % and ~23 % in the PHJ PrSCs with undoped Si NCs and p-Si NCs, correspondingly, compared to those without Si NC HEMs. The different efficacies of undoped Si NCs and p-Si NCs in the BHJ OSCs and PHJ PrSCs might be closely related with the balances of the HOMO values of the p-Si NCs and undoped Si NCs with those of the PTB7-Th and $MAPbI_3$ perovskite materials. The Si NCs HEMs increased the hole mobility in the BHJ system, facilitating the hole-extraction from the polymer to the PEDOT:PSS. These results demonstrate that the Si NCs play a key role as HEMs. We believe that the findings of this study introduce a new direction for the development of high-efficiency solution-processed BHJ OSCs and PHJ PrSCs. Further studies of effective Si NC HEM approaches of various particle sizes for high efficiency devices are on going.

## E. Reference

[1] Krebs, F. C.; *Sol. Energy. Mater. Sol. Cells*, **2009**, *93*, 394.

[2] Arias, A.C.; Mackenzie, J. D.; McCulloch, I.; Rivnay, J.; Salleo, A.; *Chem Rev.* **2010**, *110*, 3.

[3] He, Z.; Xiao, B.; Wu, H.; Yang, T.; Xiao, S.; Wang, C.; Russell, T. P.; Cao, Y.; *Nat. Photonics.* **2015**, *9*, 174.

[4] Burschka, J.; Pellet, N.; Moon, S. J.; Humphry-Baker, R.; Gao, P.; Nazeeruddin, M. K.; Grätzel, M.; *Nature*, **2013**, *499*, 316.

[5] Jeon, N. J.; Noh, J. H.; Kim, Y. C.; Yang, W. S.; Ryu, S.; Seok, S. I.; *Nat. Mater.* **2014**, *13*, 897.

[6] Liu, M.; Johnston, M. B.; Snaith, H. J. *Nature*. **2013**, *501*, 395.

[7] Meng, L.; You, J.; Guo, T. F.; Yang, T. *Acc. Chem. Res*. **2016**, *49*, 155.

[8] Jeng, J. Y.; Chiang, Y. F.; Lee, M. H.; Peng, S. R.; Guo, T. F.; Chen, P.; Wen, T. C. *Adv. Mater*. **2013**, *25*, 3727.

[9] Price, S. C.; Stuart, A. C.; Yang, L.; Zhou, H.; You, W.; *J. Am. Chem. Soc*. **2011**, *133*, 4625.

[10] Heo, J. H.; Im, S. H.; Noh, J. H.; Mandal, T. N.; Lim, C. S.; Chang, J. A.; Lee, Y. H.; Kim, H.; Sarkar, A.; Nazeeruddin, M. K.; Grätzel, M.; Seok, S. I. *Nat. Photonics*. **2013**, *7*, 486.

[11] Etgar, L.; Gao, P.; Xue, Z.; Peng, Q.; Chandiran, A. K.; Liu, B.; Nazeeruddin, M. K.; Grätzel, M. *J. Am. Chem. Soc*. **2012**, *134*, 17396.

[12] Lee, M. M.; Teushcer, J.; Miyasaka, T.; Murakami, T. N.; Snaith, H. J. *Science*. **2012**, *338*, 643.

[13] Atwater, H. A.; Polman, A. *Nat. Mater*. **2010**, *19*, 205.

[14] Zhang, W.; Saliba, M.; Stranks, S. D.; Sun, Y.; Shi, X.; Wiesner, U.; Snaith, H. J. *Nano Lett*. **2013**, *13*, 4505.

[15] Würfel, U.; Neher, D.; Spies, A.; Albrecht, S. *Nat. Commun*. **2015**, *6*, 6951.

[16] Malinkiewca, O.; Yella, A.; Lee, Y. H.; Espallargas, G. M.; Grätzel, M.; Nazeeruddin, M. K.; Bolink, H. J. *Nat. Photonics*. **2014**, *8*, 128.

[17] Zilberberg, K.; Trost, S.; Schmidt, H.; Riedl, T. *Adv. Energy Mater*. **2011**, *1*, 377

[18] Zhou, H.; Chen, W.; Li, G.; Luo, S.; Son, T. B.; Duan, H. S.; Hong, Z.; You, J.; Liu, Y.; Tang, T. *Science*. **2014**, *345*, 542.

[19] Ma, W.; Yang, C.; Hon, X.; Lee, K.; Heeger, A. J. *Adv. Funct. Mater*. **2005**, *15*, 1617.

[20] Hsu, H.; Chen, C.; Chang, J.; Yu, Y.; Shen, Y.; *Nanoscale*. **2014**, *6*, 10281.

[21] Kawano, K.; Sakai, J.; Yahiro, M.; Adachi, C.; *Sol. Energy Mater. Sol. Cells*. **2009**, *93*, 514.

[22] Lee, J. K.; Ma, W. L.; Brabec, C. J.; Yuen, J.; Moon, J. S.; Kim, J. Y.; Lee, K.; Bazan, G. C.; Heeger, A. J. *J. Am. Chem. Soc*. **2008**, *130*, 3619.

[23] Liang, P.; Liao, C.; Chueh, C.; Zuo, F.; Williams, S. T.; Xin, X.; Sin, J.; Jen, A. K. -Y. *Adv. Mater*. **2014**, *26*, 3748.

[24] Petersen, A.; Kirchartz, T.; Wagner, T. A. *Phys. Rev. B*. **2012**, *85*, 045208.

[25] Lin, Z.; Jiang, C.; Zhu, C.; Zhang, J.; *ACS Appl. Mater. Interfaces*. **2013**, *5*, 713.

[26] Liu, D.; Kelly, T. L. *Nat. Photonics*. **2014**, *8*, 133.

[27] Kyaw, A. K. K.; Sun, X. W.; Jiang, C. Y.; Lo, G. Q.; Zhao, D. W.; Kwong, D. L. *Appl. Phys. Lett*. **2008**, *93*, 21107.

[28] Huynh, W. U.; Dittmer, J. J.; Alivisatos, A. P. *Science*. **2002**, *295*, 2425.

[29] Ren, S.; Chang, L. Y.; Lim, S. K.; Zhao, J.; Smith, M.; Zhao, N.; Bulovic, V.; Bawendi, M.; Gradecak, S. *NanoLett.* **2011**, *11*, 3998.

[30] Liu, C. Y.; Holman, Z. C.; Kortshagen, U. R. *Adn. Funct. Mater*. **2010**, *20*, 2157.

[31] Ding, Y.; Gresback, R.; Liu, Q.; Zhou, S.; Pi, Z.; Nozaki, T.; *Nano Energy*. **2014**, *9*, 25.

[32] Gresback, R.; Kramer, N. J.; Ding, Y.; Chen, T.; Kortshagen, U. R.; Nozaki, T.; *ACS Nano*. **2014**, *8*, 5650.

[33] Jeong, H.; Lee, J. K.; *ACS Appl Mater. Interfaces*. **2015**, *7*, 28459.

[34] Yamani, Z.; Thompson, H.; Abu Hassan, L.; Nayfeh, H.; *Appl. Phys. Lett*. **1997**, *70*, 284559.

[35] Delley, D.; Steigmeier, E. F. *Phys. Rev. B*. **1993**, *47*, 1397.

[36] Jasieniak, J.; Califano, M.; Watkins, S. E. *ACS Nano*. **2011**, *5*, 5888.

[27] Mihalietchi, V. D.; Xie, H.; de Boer, B.; Koster, L. J. A.; Blom, P. W. M. *Adv. Funct. Mater*. **2006**, *16*, 699.

# List of Publication

1. Hanbin Jeong and Jae Kwan Lee

"Organic-Inorganic Hybrid Ternary Bulk Heterojunction of Nanostructured Perovskite-Low Bandgap Polymer-PCBM for Improved Efficiency of Organic Solar Cells"

*ACS Appl. Mater. Interfaces*. **2015**, *7*, 28459-28465

2. Hanbin Jeong, Hansol Kim, Won-Il Song, Kyung-Hoon Yoo, Jason Rama, and Jae Kwan Lee

"Improved Efficiency of Solution-Processed Bulk-Heterojunction Organic Solar Cells and Planar-Heterojunction Perovskite Solar Cells with Efficient Hole-Extracting Si Nanocrystals"

*RSC advances*. Just submitted

# List of Poster

1. Hanbin Jeong, Hansol Kim, and Jae Kwan Lee
"Ternary Bulk Heterojunction of Nanostructured Perovskite-Low Bandgap Polymer-PCBM for Improved Efficiency of Organic Solar Cells"
ICSM 2016

# Ternary Bulk Heterojunction of Nanostructured Perovskite–Low Bandgap Polymer–PCBM for Improved Efficiency of Organic Solar Cells

Hanbin Jeong, Hansol Kim, and Jae Kwan Lee*
Dept. of Chemistry Education/Carbon Materials, Chosun University, Gwangju, 61452, Republic of Korea, *E-mail: chemedujk@chosun.ac.kr

## Introduction

Organic solar cells (OSCs) fabricated by versatile printing methods such as the doctor blade, inkjet, and roll-to-roll methods are inexpensive, lightweight, and highly solution-processable. Recently solution-processed OSCs have exhibited excellent power conversion efficiency (PCE) of up to 10%. Similarly solution-processable organometal halide perovskite solar cells(PrSCs) have received considerable attention in the scientific community because the have exhibited breakthrough PCEs of over 18%. In particular, because the crystallinity, uniformity, and coverage of perovskite materials on the substrate are critical issues in improving the PCEs of devices, there has been done extensive research on developing efficient methods for the fabrication of perovskite material layers. We have also reported high-efficiency hybrid solar cells with well-organized $CH_3NH_3PbI_3$ ($MAPbI_3$) perovskite (which were fabricated under various solution processing conditions) and $PC_{71}BM$ PHJ films. Interestingly, we observed that the morphology of $MAPbI_3$ perovskite films was significantly affected by cast solvents. Thus, we have attempted to fill the polymer /PCBM BHJ composite into the sparse coverage of $MAPbI_3$ perovskite on ITO/PEDOT:PSS substrates to induce a multi-BHJ system consisting of $MAPbI_3$ perovskite/polymer/PCBM, which might be composed of polymer-PCBM, perovskite-polymer, perovskite –PCBM, or polymer-perovskite-PCBM.

## Experimental Results

### Device Fabrication

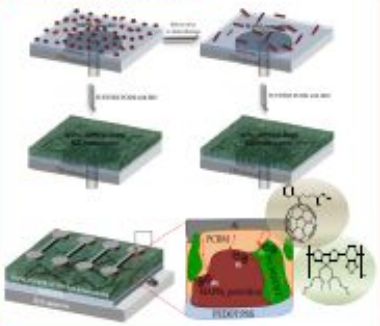

### Optimization of Devices & Surface Morphology of $MAPbI_3$ Films

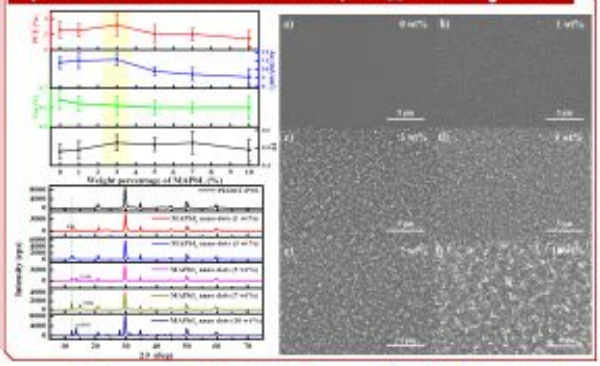

### Photovoltaic Performances

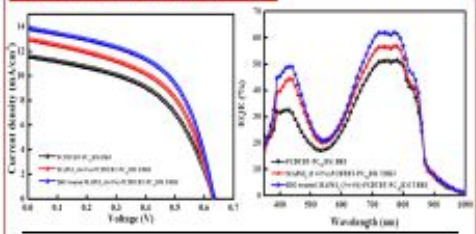

| $MAPbI_3$ | $J_{sc}$ (mAcm$^{-2}$) | $V_{oc}$ (V) | $EF$ | $\eta$ max/ave (%) |
|---|---|---|---|---|
| none | 11.6 | 0.64 | 0.51 | 3.73 / 3.58 |
| nano dots | 13.0 | 0.63 | 0.52 | 4.24 / 4.05 |
| DIO-treated nano dots | 13.9 | 0.63 | 0.55 | 4.79 / 4.47 |

### Surface Analysis of DIO Treated $MAPbI_3$ Nano dots

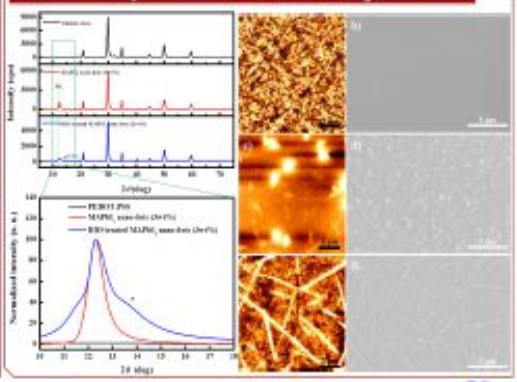

## Conclusion

- We have demonstrated high-performance TBHJ hybrid solar cells composed of nanostructured $MAPbI_3$ perovskite-PCPDTBT-PCBM.
- DIO played a key role in the development of perovskite structures of $MAPbI_3$ nano dots and induced the (110) directional crystallinity growth of the longitudinal constructive morphologies like nano rods.
- This result was reported in *ACS Appl. Mater. Interfaces* 2015, *7*, 28459-28465